Bedform development in confined and unconfined settings of the Carchuna Canyon (Alboran Sea, western Mediterranean Sea): An example of cyclic steps in shelf-incised canyons

J. Cerrillo-Escoriza [a,b,d,*], A. Micallef [c], F.J. Lobo [a], Á. Puga-Bernabéu [b], P. Bárcenas [d], I. Schulten [e,f], R. Durán [g], Á. Carrión-Torrente [a,b], A. López-Quirós [b], M. Luján [h], O. Sánchez-Guillamón [d], M.J. Sánchez [i]

[a] Department of Marine Geosciences, Instituto Andaluz de Ciencias de la Tierra (CSIC-UGR), Avenida de las Palmeras, 4, 18100 Armilla, Granada, Spain
[b] Departamento de Estratigrafía y Paleontología, Facultad de Ciencias, Universidad de Granada, Campus de Fuentenueva s.n., 18002 Granada, Spain
[c] Monterey Bay Aquarium Research Institute, 7700 Sandholdt Road, Moss Landing 95039, CA, USA
[d] Instituto Español de Oceanografía, Centro Oceanográfico de Málaga (IEO-CSIC), Explanada de San Andrés (Muelle 9), Puerto de Málaga, 29002 Málaga, Spain
[e] Marine Geology and Seafloor Surveying, Department of Geosciences, University of Malta, Triq ta' Xmiexi, Msida 37, MSD, 1803 Msida, Malta
[f] Department of Earth and Environmental Sciences, Dalhousie University, 1355 Oxford Street, B3H 4R2 Halifax, Nova Scotia, Canada
[g] Institute of Marine Sciences (CSIC), Passeig Marítim de la Barceloneta, 37-49, 08003 Barcelona, Spain
[h] Department of Earth Sciences, CASEM – Facultad de Ciencias del Mar y Ambientales, Campus Universitario de Puerto Real, Universidad de Cádiz, 11510 Puerto Real, Spain
[i] Instituto de Oceanografía y Cambio Global (IOCAG), Universidad de Las Palmas de Gran Canaria, Campus Universitario de Tafira Edif. Ciencias Básicas, 35017 Las Palmas de Gran Canaria, Spain

ARTICLE INFO

ABSTRACT

Newly acquired high-resolution multibeam bathymetry in combination with sub-bottom acoustic profiles, surficial sediment samples, and three-dimensional flow simulations made possible the characterization of bedforms along the axial channel and depositional lobe of the shelf-incised Carchuna Canyon (Alboran Sea, western Mediterranean Sea). This study aims to describe the erosional and depositional bedforms in confined and unconfined settings of the Carchuna Canyon in order to determine the genetic constraints on sedimentary processes leading to bedform development along the canyon in recent times.

The straight Carchuna Canyon, deeply incised in the shelf up to 200 m off the coastline, hosts: (1) crescentic-shaped bedforms (CSBs) that exhibit distinctive crest concavities, asymmetries, and lengths along the axial channel; (2) continuous lateral levees and; (3) a channel bend with three depressed stretches of the levee crest that are less than 20 m high. A set of concentric sediment waves and two scour trails were identified proximal to the channel bend over an overbank deposit east of the Carchuna Canyon. Four acoustic units with distinct acoustic facies were defined along the sediment wave field. The sediment transport simulation shows the highest flow velocities along the Carchuna Canyon thalweg, while over the overbank deposit the highest velocity values occur along the top of the bedform crests, with the higher Froude values being found over bedform lee sides.

The occurrence of CSBs along the canyon axial channel suggests the imprint of confined sediment-laden gravity flows descending from the canyon head and exhibiting a flow variability along the canyon induced by local variations of slope gradient and/or sediment concentration. A spatial relationship is identified between the development of sediment waves over the overbank deposit and lowered levee crest heights at the channel bend. In contrast, more energetic downstream turbiditic flows exceed the levee crest at the channel bend, focusing the overflow and promoting erosion of the overbank deposit, thereby generating the scour trains. Based on the recent history of overbank deposition, two alternating scenarios of flow behavior can be interpreted. In a high-density turbidity current setting, erosion would prevail along the axial channel. Widespread spillover flows of coarse-grained sediments would occur in both levees, forming heterogeneous sedimentary patterns that change downslope within the depositional lobe due to lesser turbulence of spillover turbidity currents and gentler slope

gradients. In contrast, in a low-density turbidity current setting, turbidity currents flowing along the Carchuna Canyon would form depositional bedforms in the axial channel, while spillover processes would be localized at the channel bend, forming either depositional or erosional bedforms over the depositional lobe according to the frequency, magnitude and focusing of turbiditic flows.

1. Introduction

Submarine canyons can transport large volumes of terrigenous material from the continent to the deep-sea environment and are the primary conduits of source-to-sink systems (Sømme et al., 2009; Nyberg et al., 2018; Bührig et al., 2022). The morphology of submarine canyons is the product of multiple oceanographic and sedimentary processes, particularly of turbidity currents and slope failures (Shepard, 1981; Pratson et al., 1994; Fabri et al., 2017; Saldías and Allen, 2020; Talling et al., 2022; Brun et al., 2023; Dobbs et al., 2023). The formation of turbidity currents and associated downslope sediment transport along submarine canyons may be induced by processes that include fluvially-derived hyperpycnal flows (Mulder and Alexander, 2001; Mas et al., 2010; Martinez-Lamas et al., 2020), storms (Smith et al., 2005; Paull et al., 2011; Xu et al., 2013; Bosman et al., 2020), and enhanced off-shelf advection (Palanques et al., 2008). Downcanyon sediment transport can also be triggered by the failure of recently deposited fluvial sediments (e. g., Mulder and Alexander, 2001; Mas et al., 2010) or by canyon flank failures (e.g., Goldfinger et al., 2007; Vangriesheim et al., 2009; Micallef et al., 2012). Oceanographic processes such as dense shelf-water cascading (e.g., DeGeest et al., 2008; Palanques et al., 2012; Saldías and Allen, 2020) and internal waves also contribute to particle dispersal within canyons (e.g., Xu et al., 2010; Puig et al., 2013, 2014; Droghei et al., 2016; Maier et al., 2019).

Relationships between characteristics of source-to-sink systems and canyon geomorphology are demonstrated in a number of regional-scale studies (e.g., Lastras et al., 2007; Jipa and Panin, 2020; Bührig et al., 2022; Fernane et al., 2022) where sediment transport along submarine canyons is recorded by the overall curvature of longitudinal profiles (Gerber et al., 2009) and a variety of superimposed, smaller-scale morphologies, such as bedforms, terraces, knickpoints, gullies and scars (e.g., Hagen et al., 1994; Peakall et al., 2000; Wynn and Stow, 2002; Baztan et al., 2005; Mitchell, 2006; Lastras et al., 2007; Mountjoy et al., 2009; Tubau et al., 2013; Micallef et al., 2014; Symons et al., 2016). The spatial variability of bedforms along submarine canyons is particularly noteworthy, as a reflection of the recurrent passage of turbidity currents (Peakall et al., 2000; Fildani et al., 2006; Kostic, 2011; Covault et al., 2014, 2017). These bedforms have different morphological features depending on the prevalence of deposition or erosion, such as sediment waves or scours (Symons et al., 2016; Covault et al., 2017; Slootman and Cartigny, 2020), and the confined or unconfined nature of the canyon setting, which may display axial channels, levees, or depositional lobes (e.g., Tubau et al., 2015; Hage et al., 2018).

Coarse-grained, crescentic-shaped bedforms (CSBs) are usually confined along the axial channel of submarine canyons (e.g., Smith et al., 2005, 2007; Xu et al., 2008; Kostic, 2011; Paull et al., 2011, 2013; Babonneau et al., 2013; Covault et al., 2014; Mazières et al., 2014; Tubau et al., 2015; Sun et al., 2023). Confined CSBs typically develop in net-erosion or low-aggradation rate settings (Smith et al., 2007; Paull et al., 2010; Hughes Clarke et al., 2014). The imbalance between erosion on the lee side and deposition on the stoss side of CSBs often leads to their upslope migration (Tubau et al., 2015; Slootman and Cartigny, 2020), generally in response to relatively brief, high-energy turbidity flow events (Normark et al., 2002; Smith et al., 2005; Xu et al., 2008; Paull et al., 2010; Babonneau et al., 2013; Symons et al., 2016; Hage et al., 2018; Sun et al., 2023).

Bedform development is more diverse in unconfined settings of submarine canyon systems, such as backslopes of channel levees, where sediment waves and scours can be found (e.g., Migeon et al., 2000, 2001; Wynn et al., 2000, 2002; Normark et al., 2002; Fildani et al., 2006; Arzola et al., 2008; Kostic, 2014; Symons et al., 2016; Ge et al., 2017; Casalbore et al., 2018; Li and Gong, 2018; Maselli et al., 2019, 2021; Stacey et al., 2019; Zhou et al., 2021; Normandeau et al., 2022; Scacchia et al., 2022). The development of these bedforms also depends on the relationship between erosion and deposition (Symons et al., 2016). Net-depositional fine-grained sediment waves are characterized by positive reliefs with straight to sinuous plan-view shapes (Zhong et al., 2015; Symons et al., 2016). In contrast, scours are predominantly net-erosional bedforms that occur as isolated depressions or linear trains. They are characterized by crescent-shaped to closed depressions that cut into the seafloor and often form asymmetrical waveforms (Fildani et al., 2006; Macdonald et al., 2011; Covault et al., 2014; Paull et al., 2014; Zhong et al., 2015).

Sediment waves and scours can be interpreted as cyclic steps. These are upstream-migrating bedforms in regions with high gradients and slope breaks (Kostic, 2011; Tubau et al., 2015; Hage et al., 2018), where each individual bedform along a field is bounded by hydraulic jumps of an overriding turbidity current that is Froude-supercritical over the steep lee side and Froude-subcritical over the smooth stoss side (Covault et al., 2014). Cyclic steps can be found in both confined and unconfined submarine canyon settings (Paull et al., 2011; Zhong et al., 2015) and have a key role in canyon initiation and maintenance (Fildani et al., 2013; Hizzett et al., 2017; Slootman and Cartigny, 2020; Ono et al., 2023) as they can significantly enhance sediment transport efficiency (Sun and Parker, 2005; Taki and Parker, 2005; Slootman and Cartigny, 2020). The geometric properties of cyclic steps (i.e., wavelength, amplitude, and asymmetry) are controlled by factors that include canyon floor gradient, flow thickness, and flow velocity (Cartigny et al., 2011; Kostic, 2011; Slootman and Cartigny, 2020).

Present understanding of how the currents transport sediments and form the cyclic steps mainly derives from interpreting their deposits (turbidites), together with laboratory-scale (flume) experiments and numerical modelling (e.g., Spinewine et al., 2009; Talling et al., 2012; Basani et al., 2014; Cartigny et al., 2014; Kostic, 2014; Vellinga et al., 2016, 2018; Vellinga, 2019; Hage et al., 2018). These methods have produced major advances in understanding sedimentary activity, but until recently there were very few direct measurements of turbidity currents in action and the migration of cyclic steps (Lo Iacono et al., 2020). Numerical models have provided valuable insight into the development and mechanics of cyclic steps, by exploring how average flow velocity, sediment concentration, and flow thickness vary over the length of the bedform wavelength (e.g., Fildani et al., 2006; Kostic and Parker, 2006; Kostic et al., 2010; Kostic, 2014; Cartigny et al., 2011; Covault et al., 2014, 2016). However, few studies that show physical and numerical modelling of flow with the development of recent bedforms in submarine canyons have been tackled yet (e.g., Chen et al., 2021).

The straight shelf-incised Carchuna Canyon crosses the entire shelf in the northern Alboran Sea (western Mediterranean Sea) and exhibits bedforms both in confined and unconfined settings, along its axial channel and above an overbank deposit. Based on the characterization of erosional and depositional bedforms in the submarine canyon environment, the objectives of our study are: (1) to decipher genetic processes and controlling factors leading to the formation of bedforms in confined and unconfined settings of submarine canyons; and (2) to determine bedform development, maintenance or demise and, by extension, canyon activity in recent times.

2. Regional setting

The shelf-incised Carchuna Canyon is located in the central sector of the northern Alboran Sea margin, between Motril and Carchuna towns, in front of Cape Sacratif (Fig. 1). The Alboran Sea is a narrow and elongated basin located in the westernmost part of the Mediterranean Sea (Fig. 1A). The basin formed as a result of various tectonic processes during the Neogene, in the wake of continental collision between the African and European plates (Platt and Vissers, 1986; Comas et al., 1992). These processes influenced the morpho-structure of the basin, which exhibits a complex present-day physiography (Ballesteros et al., 2008).

2.1. The coastal domain

Sediment input to the coastline of the northern Alboran Sea is mainly provided via relatively short mountain streams (Liquete et al., 2005) and ephemeral creeks, active only in autumn and winter (Stanley et al., 1975; Fabres et al., 2002; Palanques et al., 2005). Inshore of the Carchuna Canyon, two small river beds with a torrential character during the rainy season discharge in the proximity of the study area: Villanueva Ravine inland from the Motril Canyon, and Gualchos Ravine east of the study area. Both are short (<20 km), have high slopes (>3.6°), and occur in small basins (<120 km²) (Bárcenas et al., 2009). The Guadalfeo River, a major regional fluvial system, lies west of the study area (Fig. 1B).

The coastal sedimentary record adjacent to the Carchuna Canyon head comprises alluvial fans with conglomerates formed from the Late Pleistocene to the Middle Holocene (Lario et al., 1999; Fernández-Salas et al., 2009), and sandy deposits —spit bars and infralittoral prograding wedges (IPWs)— generated by coastal drift and storm-driven sediment transport during the Holocene (Lario et al., 1999; Fernández-Salas et al., 2009; Bárcenas et al., 2011).

2.2. Submarine landforms and processes

The shelf of the northern Alboran Sea is narrow (2–15 km wide), with the shelf break located at an average water depth of 115 m (Ercilla et al., 1994; Vázquez, 2001). The study area comprises the narrowest shelf (2 km) of the entire northern margin, having a gradient of less than 1° (Fig. 1) (Ercilla et al., 1994; Fernández-Salas et al., 2009). The western sector of the shelf in the study area is characterized by the southeastward trending Guadalfeo River deltaic system (Fig. 1B) (Bárcenas et al., 2015; Lobo et al., 2015). In the central and eastern parts of the shelf within the study area, several generations of coarse-grained IPWs have been identified (Fig. 1C), upon which the Carchuna Canyon head is incised (Fernández-Salas et al., 2009; Ortega-Sánchez et al., 2014). The Carchuna IPW is fed by ephemeral streams between Carchuna and Calahonda towns, as well as by littoral drift cells (Ortega-Sánchez et al., 2014).

The shelf-to-slope transition around the study area is marked by diverse erosive features composing turbiditic systems. Specifically, the Sacratif Turbidite System includes the Motril and Carchuna submarine canyons (Fig. 1B, C) (Pérez-Belzuz and Alonso, 2000). The Motril Canyon is located 5 km southeast of the Guadalfeo River mouth at 70 m water depth, and its main valley exhibits a sinuous morphology on the
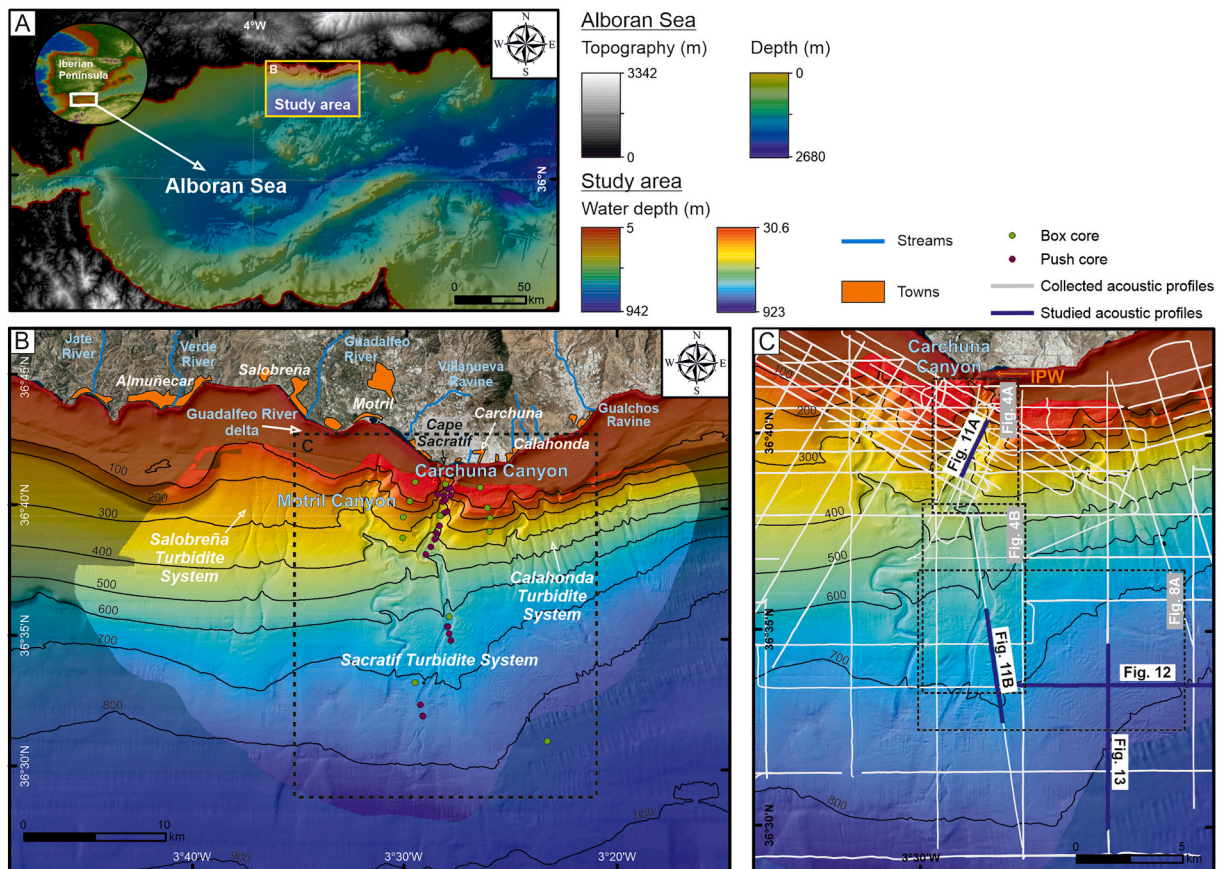

Fig. 1. (A) Geographical location of the study area in the southern Iberian Peninsula. Overview of the Alboran Sea indicating the study area in the northern margin. (B) 10 m high-resolution bathymetric map constructed with data collected during the ALSSOMAR-S2S survey superimposed to a 50 m cell bathymetric grid, provided by the "Ministerio de Pesca y Agricultura", Spanish Government. The map shows the Carchuna Canyon and the location of sediment cores collected in the canyon during the oceanographic survey ALSSOMAR-S2S. (C) Zoomed-in high-resolution bathymetric map of the study area showing the location of acoustic profiles collected, and the location of Figs. 4A, C, 8A, 11, 12, and 13. IPW: Infralittoral Prograding Wedge. Bathymetric contours in meters.

slope (Cerrillo-Escoriza et al., 2024). The straight Carchuna Canyon crosses the shelf and its canyon head is located 200 m off Cape Sacratif at 25 m water depth (Cerrillo-Escoriza et al., 2024). Both canyons discharge into large lobes fed by distributary channels (Pérez-Belzuz and Alonso, 2000; Pérez-Belzuz et al., 2000) and host superimposed sediment wave fields whose formation has been related to sediment fluxes along the axial channel and eventual spillover above meanders of the Carchuna Canyon (Muñoz et al., 2017).

In the deep Alboran Sea, sediment accumulations are mostly driven by hemipelagic processes (Masqué et al., 2003), although sediment transport along the slopes, base-of-slopes, deep basin, and seamount flanks (Ercilla et al., 2016) is also governed by near-bottom currents (Fabres et al., 2002).

2.3. Oceanographic setting

The coast in the study area is affected by wave trains coming from W, WSW, SW, ESE and E, oblique to the main E-W coastal trend (Ortega-Sánchez et al., 2014). The Carchuna Canyon head (25–250 m water depths) influences the coastal swell and storm-related processes by increasing nearshore wave heights, particularly of western waves, favoring long-term coastal erosion due to energy concentration (Ortega-Sánchez et al., 2014). The shelf around the Carchuna Canyon head is affected by currents with velocities of >0.1 m·s^{-1} in the upper layer under the dominance of easterlies. Under the dominance of westerlies, the upper layer shows current velocities towards the northeast of <0.1 m·s^{-1} (Bárcenas et al., 2011). A bottom flow showing patterns different from the wind-driven surface current has been detected in the Carchuna Canyon. In the bottom layer, currents tend to flow downcanyon, especially during easterlies dominance, with flow velocities between 20 and 30 cm·s^{-1} (Serrano et al., 2020).

3. Methodology

Datasets used for this study were collected during the ALSSOMAR-S2S oceanographic expedition carried out from 29 August to 19 September 2019, on board RV "Sarmiento de Gamboa" in the continental shelf and slope of the northern Alboran Sea between Almuñecar Town and east of Gualchos Ravine (Fig. 1).

3.1. Multibeam bathymetric data

A multibeam bathymetric data set was collected across the study area using a hull-mounted Atlas Hydrosweep DS™ multibeam echo sounder operating at frequencies of 14.5 to 16 kHz, which provides data coverage of up to six times the water depth. Raw multibeam data were processed with Caris™ HIPS and SIPS software to generate a 10 m cell size grid. Post-processing of multibeam bathymetric data was conducted in order to reduce artefacts generated during data acquisition. Specifically, different vertical errors were detected to have occurred during acquisition, apparently due to incorrect application of sound velocity profiles. These artefacts were manually corrected by adjusting the vertical reference of adjacent bathymetric lines. This type of processing and cleaning involved the loss of data points but enabled the removal of artefacts. In the case of relatively small vertical gaps, smoothed interpolations were applied. In addition, processing steps also included the application of tidal correction, ribbing reduction (i.e., removal of motion artefacts) and manual correction of spikes. Processed bathymetric data were used to generate different digital terrain models in ASCII xyz and GeoTiff formats, with cell size resolutions of 30, 20, and 10 m. These data were imported in a geographic information system (ArcGIS™) (Fig. 1B, C) to be used as a base map into which the other data were integrated. Multibeam bathymetric data served to determine the spatial variability of bedforms identified in canyon longitudinal profiles and to calculate canyon morphometric parameters (e.g., maximum canyon width, depth range, sinuosity index, and maximum relief).

The major geomorphological features of the Carchuna Canyon include the axial channel, terraces and canyon flanks (canyon terminology based on Paull et al., 2013). Geomorphological segments in the Carchuna Canyon were defined according to the orientation of the axial channel and the slope of the flanks. Bathymetric profiles along the Carchuna Canyon thalweg were classified according to Covault et al. (2011). The main geomorphic parameters used to characterize sediment waves include amplitude, wavelength, and slope of lee and stoss sides; for the characterization of scours, scour width, length, and headwall height were determined (See supplementary material 1) (bedform terminology based on Tubau et al., 2015). Sets of CSBs (designed by letters) were defined in view of CSB crest concavity, considered as high (≥ 0.6) or low (<0.6) according to the length/width ratio. In addition, two sectors of unconfined sediment waves were defined according to their distinctive wavelengths and heights. Bedform asymmetry was determined using the methodology outlined by Xu et al. (2008), which includes the following steps: (1) selection of downcanyon bathymetric profiles, (2) profile detrending, (3) calculation of the first derivative, (4) calculation of the ratio H/L (height/wavelength) based on the first derivative function, and (5) calculation of the asymmetry index for each undulation/bedform. A positive index indicates upcanyon asymmetry, whereas a negative index indicates downcanyon asymmetry.

3.2. Sub-bottom profiles

Sub-bottom acoustic profiles collected by means of a Teledyne Parasound™ PS-35 echo sounder were used in this study (Fig. 1C). The echo sounder operated with a primary frequency of 18 kHz and a secondary frequency of 4 kHz, resulting in maximum penetrations of about 0.1 s TWTT (Two-Way Travel Time) with a vertical resolution of up to 15 cm. Processed SEG-Y files (static corrections, gains, and spike removal) were imported in IHS Kingdom™ software for subsequent interpretation.

3.3. Seafloor sediment samples

A total of 19 sediment cores up to 30 cm long were collected with a push corer mounted on the Remote Operating Vehicle (ROV) Luso (EMEPC—Portuguese Task Group for the Extension of the Continental Shelf), and handled by an applier arm (Fig. 1B). High- and low-resolution photos and video footage were acquired in several dives by means of a standard definition video camera Argus HD-SDI 1/3″ mounted on the ROV. The ROV Luso was equipped with laser pointers having a laser beam spacing of 62 cm to provide a scale reference, and an ultra-short baseline positioning system to ensure detailed records of the ROV tracks. Additionally, 13 sediment cores up to 50 cm long were collected by deploying a box corer from the vessel (Fig. 1B). Although longer sediment cores, especially in the depositional lobe, could provide a better understanding of sedimentary processes, their number and recovery during the ALSSOMAR-S2S oceanographic expedition were very limited and could not be used to assist in the characterization of bedforms in the submarine canyon environment.

Sediment cores were split and a visual description of sedimentary facies (colour, grain size, lithology, texture, bioturbation) was undertaken. Grain size analysis was carried out on the uppermost centimeter of 23 sediment cores using 10–15 g of dried sediment (60 °C) pre-treated with 20 % H$_2$O$_2$ to remove organic matter, and sodium hexametaphosphate as a dispersing agent. Samples were wet sieved to separate the coarse fraction (gravel) using a 2 mm mesh size sieve. Particles <2 mm (sand, silt, and clay) were measured using a laser diffraction analyser (Mastersizer 3000, Malvern®). The textural classification of the sediments was based on Folk (1954) ternary diagrams.

3.4. Three-dimensional flow simulation

The software *FLOW-3D*® HYDRO (Version 2022R1) was used to simulate different three-dimensional flow scenarios. Previous studies

successfully used this software to simulate turbidity currents to study the generation and instability of cyclic steps in open channel flows (e.g., Basani et al., 2014; Vellinga et al., 2016, 2018; Vellinga, 2019; Ge et al., 2017). FLOW-3D® Version 2022R1 [FLOW-3D HYDRO] (2022) uses computational fluid dynamic (CFD) modelling based on the Reynolds Averaging Navier-Stokes (RANS) approach (see www.flow3d.com). This approach considers the mass-conservation and momentum-conservation equations, which enables the description of fluid motion, solve time-averaged equations, and use a turbulence model to approximate the small-scale turbulence (e.g., Heimsund et al., 2002; Vellinga et al., 2018; Vellinga, 2019). This software can use multibeam bathymetric data to reconstruct flow velocities and the Froude number.

We choose a mesh cell size of 20 m to simulate water flows along the Carchuna Canyon. The following physical models, provided within the FLOW-3D software, were chosen for the simulation: shallow-water model (viscous bed shear stress and turbulent bed shear stress enabled); gravity and non-inertial model (gravitational acceleration in z-direction = 9.81 m·s^{-2}); turbulence and viscosity model (renormalized group or RNG model to calculate wall shear stress where turbulence mixing length is dynamically computed); and variable density flow model (2nd order monotonicity preserving approximation to density transport equation). Specific settings (e.g., momentum equation) within the software were left at their default settings. More information on the physical models can be found in Basani et al. (2014) and Vellinga (2019). For simplification, no submerged flow was considered, and the seafloor was treated as a non-erosional solid medium. This setup of the simulation therefore does not fully imitate the actual conditions of a submerged sediment flow and instead considers a denser sediment flow along a non-submerged surface, which may limit the reliability of our simulation. Our simulation does not further consider any erosion or deposition and thus there is no modification to the existing bathymetry that could alter the sediment flow over long-time scales. Given that we intended to study sediment flow along the current bathymetric setting for a short time scale to retrieve information about the initial flow thickness and flow behavior, we do not consider this a limitation to our simulation. The simulation setting yields velocity values that appear too high for submarine environments (up to 45 m·s^{-1}). For this reason, the results only distinguish high and low flow velocities. Different flow initiation heights at the canyon head were tested, which resulted in different flow behavior along the canyon thalweg. The simulation enabled us: (1) to determine the initial flow thickness needed to over-flow the bedform areas; (2) to discern the occurrence of a single over-flow or of multiple overflow events. The simulation results reveal that once a minimum flow thickness is attained, the three bedform areas can be overflowed simultaneously, and that the overflows exhibit different Froude numbers in each area. For the final simulation, the height of fluid flow at the canyon head was set to 30 m, as this height produced flow results that agree well with field observations. Flow 3D post v1.1 was used for postprocessing the data.

4. Results

4.1. Geomorphology and sedimentology of the Carchuna Canyon

The shelf in the study area is up to 3 km wide, narrowing due to the occurrence of shelf-incised canyon heads (Figs. 1 and 2). Shelf surficial sediments close to the Carchuna Canyon head consist of very fine sands (Fig. 2).
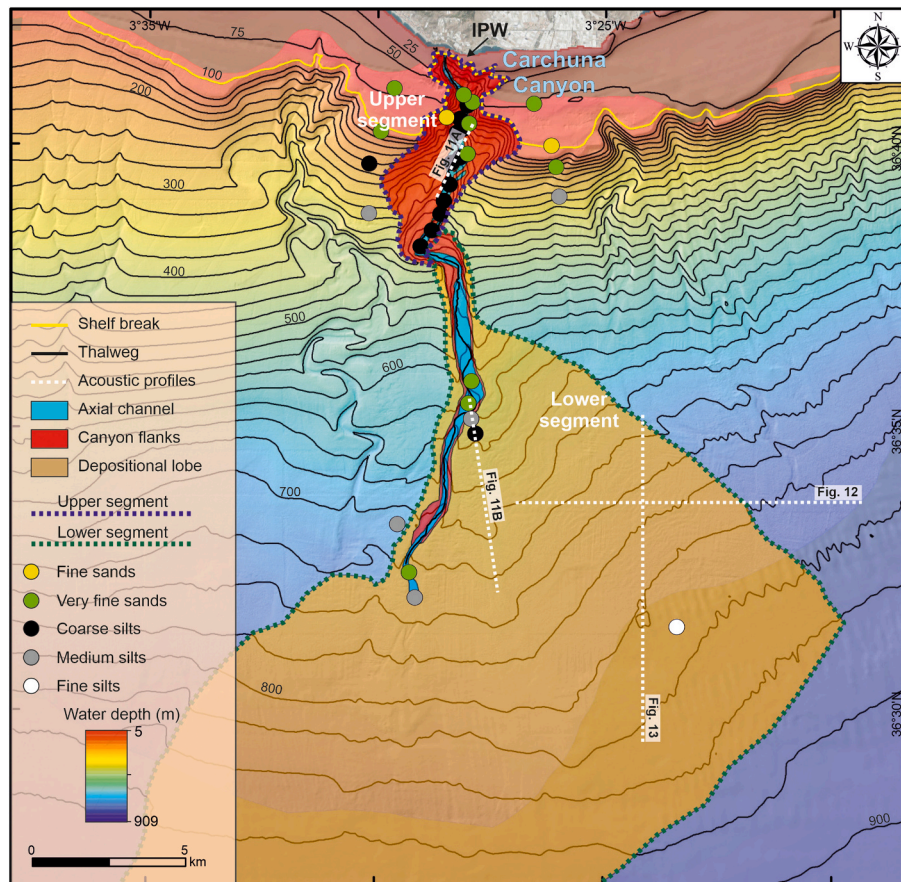

Fig. 2. Geomorphological map of the Carchuna Canyon showing the segment distribution and the texture of surficial sediment samples. The location of interpreted acoustic profiles is also shown. Note the change in orientation of the valley in the transition from the upper to the lower segment. IPW: Infralittoral Prograding Wedge. Bathymetric contours in meters.

The Carchuna Canyon has a length of 20.3 km from the canyon head to the mouth and displays an axis with a sinuosity of 1.15. It has a maximum width of 4 km and a maximum relief of 226 m (Table 1). Its longitudinal profile is concave (Fig. 3). Two geomorphological segments can be identified in the Carchuna Canyon (Fig. 2). In the upper segment (30–500 m water depths), the canyon is deeply incised in the shelf (Figs. 2 and 3B); its head, located just 200 m off the coastline, features a 100 m wide axial channel delimited by very steep flanks (68°). The canyon is straight in this segment, where the axial channel widens up to 300 m from 370 m to 430 m water depth and is limited by a narrow and steep eastern flank and large terraces on the western flank (Fig. 4A). Sediments on the axial channel comprise very fine sands in the canyon head, changing downcanyon to coarse silts (Fig. 2). The transition between the upper and lower segments is marked by an abrupt change in orientation of the main valley from NNE-SSW to WNW-ESE (Fig. 2).

The lower segment (500–730 m water depths) is characterized by a straight and wide valley (up to 550 m wide) with a main N-S orientation, an axial channel bounded by steep walls (ca. 20°) and continuous lateral levees (Figs. 2, 3B and 4B). The axial channel is straight but exhibits a bend at 620 m water depth that shifts from NNW-SSE to NNE-SSW orientation (Figs. 2 and 5). Overall, the height between the eastern levee crest and the thalweg decreases from 90.6 m in the upper reaches of the lower segment (ca. 500 m water depth) to 3.5 m at the termination of the channel (ca. 730 m water depth) (Fig. 5A). However, three stretches (upper, middle and lower) along the channel bend between 585 and 645 m water depths in the levee crest exhibit levee heights below 20 m that are separated by heights up to 28 m (Fig. 5B, C). Upslope of the channel bend, the levee height is 18.7 m between 591 and 600 m water depths (Fig. 5B, C). The levee is 19.9 m high where the axial channel changes its orientation between 611 and 621 m water depths. This middle stretch is separated from the upper and lower stretches by

26–28 m high levees (Fig. 5B, C). Downslope, the lower stretch of the channel bend between 631 and 642 m water depths exhibits a 17.6 m high levee (Fig. 5B, C). The eastern levee evolves downslope to an overbank deposit having superimposed features that extend up to 900 m water depth, forming a depositional lobe (Fig. 2). Sediments in the lower segment vary from very fine sands in the axial channel to fine silts in the depositional lobe (Fig. 2).

4.2. Fine-scale morphology of the Carchuna Canyon

A total of 111 crescentic-shaped bedforms (CSBs) were observed along the axial channel of the upper segment from 96 to 496 m water depths. These CSBs have wavelengths from 10 to 120 m and amplitudes between 1 and 9 m. The lee sides of the CSBs exhibit gradients between 2.5 and 11.3°, while the stoss sides dip between 0.2 and 5.9° (Table 1). CSBs are grouped in 12 sets of 5 to 17 CSBs, ranging in length from 310 m to 730 m (Figs. 3 and 4; Table 1). CSB sets have distinctive crest concavities, asymmetries and lengths. Overall, the CSB sets with high concavity (length/width > 0.6) associated with high seafloor slope gradients (sets *b*, *c*, *e*, *f*, *h*, and *k*; Figs. 3, 4 and 6A; Table 1) alternate with CSB sets of low concavity downcanyon (length/width < 0.6) associated with lower slope gradients (sets *a*, *d*, *g*, *i*, *j*, and *l*; Figs. 4 and 6A; Table 1). In the upper segment, most CSBs show a preferred downcanyon-directed asymmetry (Fig. 7A, B).

A total of 96 CSBs with wavelengths between 20 and 140 m and amplitudes from 1 to 5 m were identified along the axial channel of the lower segment from 502 to 704 m water depths. There, CSBs lee side gradients vary between 2.1° to 8.4°, while stoss sides are longer and their gradients vary between 0.1 and 2.4° (Table 1). In the lower segment, CSBs are grouped in 10 sets (Figs. 3 and 4; Table 1) of 4 to 17 CSBs that extend between 430 and 1340 m (Fig. 4). As in the upper

Table 1
Morphological parameters of Carchuna Canyon crescentic-shaped bedforms.

Carchuna Canyon		
	Longitude (W)	3° 28′ 34.34″
	Latitude (N)	36° 41′ 41.02″
	Total length (m)	20,366
	Sinuosity	1.15
	Maximum width (m)	4020
	Maximum incision (m)	226

Sets of CSBs of the upper segment	a	b	c	d	e	f	g	h	i	j	k	l	Total	a'
Length of the set (m)	310	510	510	410	490	590	540	600	570	730	530	720		610
Number	7	9	8	11	11	11	8	5	5	17	7	12	111	8
Wavelength (m)	20 to 60	30 to 90	30 to 90	10 to 60	20 to 60	20 to 70	30 to 80	90 to 120	40 to 100	20 to 80	40 to 80	30 to 80	10 to 120	40 to 100
Amplitude (m)	1 to 5	1 to 4	2 to 9	1 to 4	1 to 4	1 to 6	2 to 4	4 to 9	2 to 4	1 to 5	1 to 3	1 to 4	1 to 9	7 to 12
Lee side (°)	5.2 to 10.4	4.1 to 7.3	5.1 to 8.8	4.2 to 8.5	3.2 to 11.3	2.5 to 10.2	4.7 to 8.8	6.1 to 8.8	2.7 to 5.3	3.4 to 6.4	3 to 7.1	2.5 to 6.5	2.5 to 11.3	9.6 to 13.8
Stoss side (°)	1.2 to 3.9	1.7 to 4	3.8 to 5.9	2.5 to 4.5	0.5 to 4.4	0.8 to 4.2	0.6 to 3.3	0.3 to 4.1	0.4 to 1	0.9 to 4.5	0.7 to 1.7	0.2 to 3	0.2 to 5.9	4 to 9.5
Average concavity	0.37	0.61	0.64	0.43	0.68	0.62	0.29	0.64	0.57	0.43	0.75	0.25		0.58
Average gradient	4.9	5.2	7.2	4.6	5	4.6	3.9	3.6	2.6	3.6	3.2	2.7		9.5

| Sets of CSBs of the lower segment	q	r	s	t	u	v	w	x	y	z	Total
Length of the set (m)	1230	840	1340	780	960	490	760	510	890	430	
Number	17	12	14	11	12	7	10	4	4	5	96
Wavelength (m)	30 to 120	30 to 120	30 to 140	30 to 90	30 to 100	30 to 100	20 to 120	100 to 120	50 to 130	70 to 100	20 to 140
Amplitude (m)	1 to 4	1 to 3	1 to 5	1 to 2	1 to 3	1 to 2	1 to 3	1 to 3	1 to 5	1	1 to 5
Lee side (°)	3.2 to 8.4	2.5 to 5.7	2 to 6	2.1 to 4	3 to 4.6	2.4 to 4.2	2.8 to 7.5	3.4 to 5.6	3.2 to 7.5	3.4 to 4.2	2.1 to 8.4
Stoss side (°)	0.1 to 2.9	0.2 to 2.4	0.1 to 1.6	0.1 to 1.6	0.2 to 1.7	0.2 to 1.3	0.1 to 1.7	0.1 to 1.2	0.5 to 1.5	0.2 to 1	0.1 to 2.4
Average concavity	0.50	0.67	0.53	0.40	0.86	0.60	0.86	0.70	0.44	0.96	
Average gradient	2.9	2.6	2.1	1.7	2	2	3.1	2.3	2	2.1	
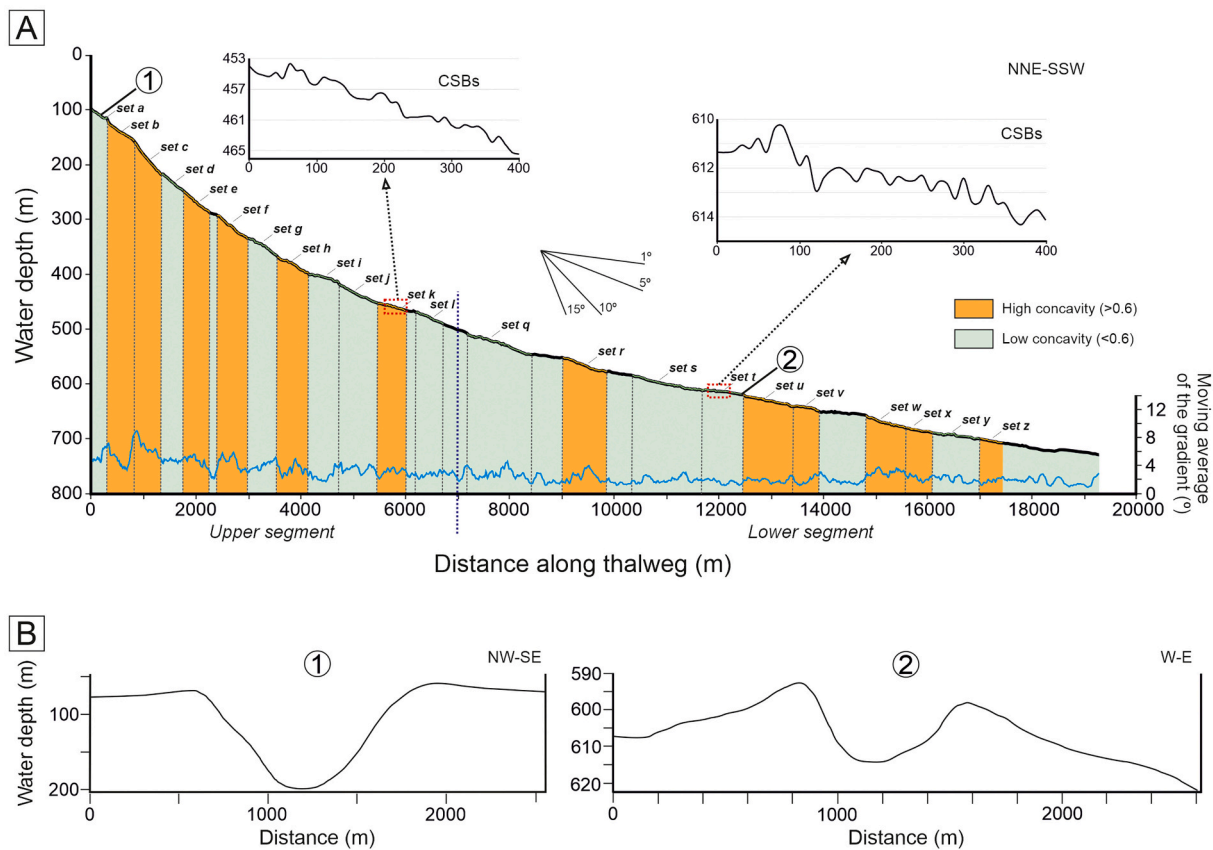
Fig. 3. (A) Bathymetric longitudinal profile and moving average (10 points) of the Carchuna Canyon thalweg gradient with indication of each CSB set according to its concavity. Zoom-ins of two sectors located in the upper and lower segments are provided. CSBs: crescentic-shaped bedforms. (B) Transverse profiles showing the shelf incision of the Carchuna Canyon in the upper segment (1) and the lateral levees in the lower segment (2). Location of transverse profiles indicated in Fig. 3A. Note that the eastern levee exhibits lower values of height than the western levee, forming an asymmetric cross section.

segment, there is an alternation between CSB sets that exhibit high concavity (length/width > 0.6) associated to high seafloor gradients (sets *r, u, v, w, x,* and *z*; Figs. 4 and 6B) and CSB sets with low concavity (length/width < 0.6) associated with lower slope gradients (sets *q, s, t,* and *y*; Figs. 4 and 6B; Table 1). In this lower segment, most of the CSBs show a preferred upcanyon-directed asymmetry (Fig. 7C, D).

Two types of bedforms were identified over the overbank deposit east of the lower canyon segment: sediment waves and scours (Fig. 8). A sediment wave field was mapped over an area of 57 km² between 555 and 805 m water depths, with a mean seafloor gradient of 2°. The main orientation of the sediment wave crests is NW-SE (Fig. 8B, C). Two sectors (upper and lower) were identified in the sediment wave field according to differences in wavelength and amplitude (Figs. 8C and Supplementary material 2). In the upper sector, between 625 and 700 m water depths, the average wavelength of the sediment waves is 106 m, with a maximum wavelength of 350 m. They have average and maximum amplitudes of 6.2 m and 15 m, respectively (Figs. 8C and Supplementary material 2 A, B). Additionally, sediment waves in this sector exhibit a downcanyon asymmetric trend (Fig. 9A, B). In the lower sector (between 700 and 800 m water depths), the average wavelength of the sediment waves is 146 m, with a maximum wavelength of 380 m. Here, sediment waves have an average amplitude of 4.9 m and a maximum amplitude of 9 m (Figs. 8C and Supplementary material 2C, D) and an upcanyon asymmetric trend (Fig. 9A, C).

Two trains of N-S oriented scours are located over the eastern overbank deposit between the upper sector of the sediment wave field and the Carchuna axial channel at 623 to 711 m water depths (Fig. 8). In plan view, these scours display parallel to divergent limbs and crescentic depressions at the base of headwall scarps (Fig. 8B, D). The shallowest

train of scours occurs between 623 and 678 m water depths and comprises 13 scours extending along 2600 m (Figs. 8D and Supplementary material 2E). Individual scours range from 130 to 280 m in width, from 70 to 180 m in length, and from 2 to 8 m in headwall height (Fig. 10A). The sidewalls and the depressions display slopes of 1° to 5°; sub-surface sediments are characterized by homogeneous sandy muds with thin interbedded fine sands (Fig. 10A, C). In contrast, the steepest gradients (6° to 12.6°) occur on the headwalls, which are characterized by strong changes in the slope gradients and erosional features such as furrows, while the sub-surface sediments exhibit homogeneous sandy muds with very dispersed clasts of very coarse sands (Fig. 10). The deepest train occurs between 681 and 711 m water depths and is formed by 8 scours, extending 1420 m (Figs. 8D and Supplementary material 2F). Individual scours range from 60 to 190 m in width, from 15 to 80 m in length, and from 1 to 8 m in headwall height. The sidewalls and the depressions have slopes of 1° to 4°, while the steepest gradients (5° to 9°) occur on the headwalls.

4.3. Sub-surface acoustic facies and architecture of Carchuna Canyon bedforms

4.3.1. Description of acoustic facies

Five acoustic facies were distinguished along the Carchuna Canyon (Table 2). *Acoustic facies a* is characterized by a transparent configuration. *Acoustic facies b* exhibits low- to moderate-amplitude continuous and parallel reflections. *Acoustic facies c* features moderate- to high-amplitude discontinuous undulating reflections; internal reflections stack vertically with asymmetric shapes. *Acoustic facies d* exhibits high-amplitude parallel to gently undulating reflections. *Acoustic facies e* is
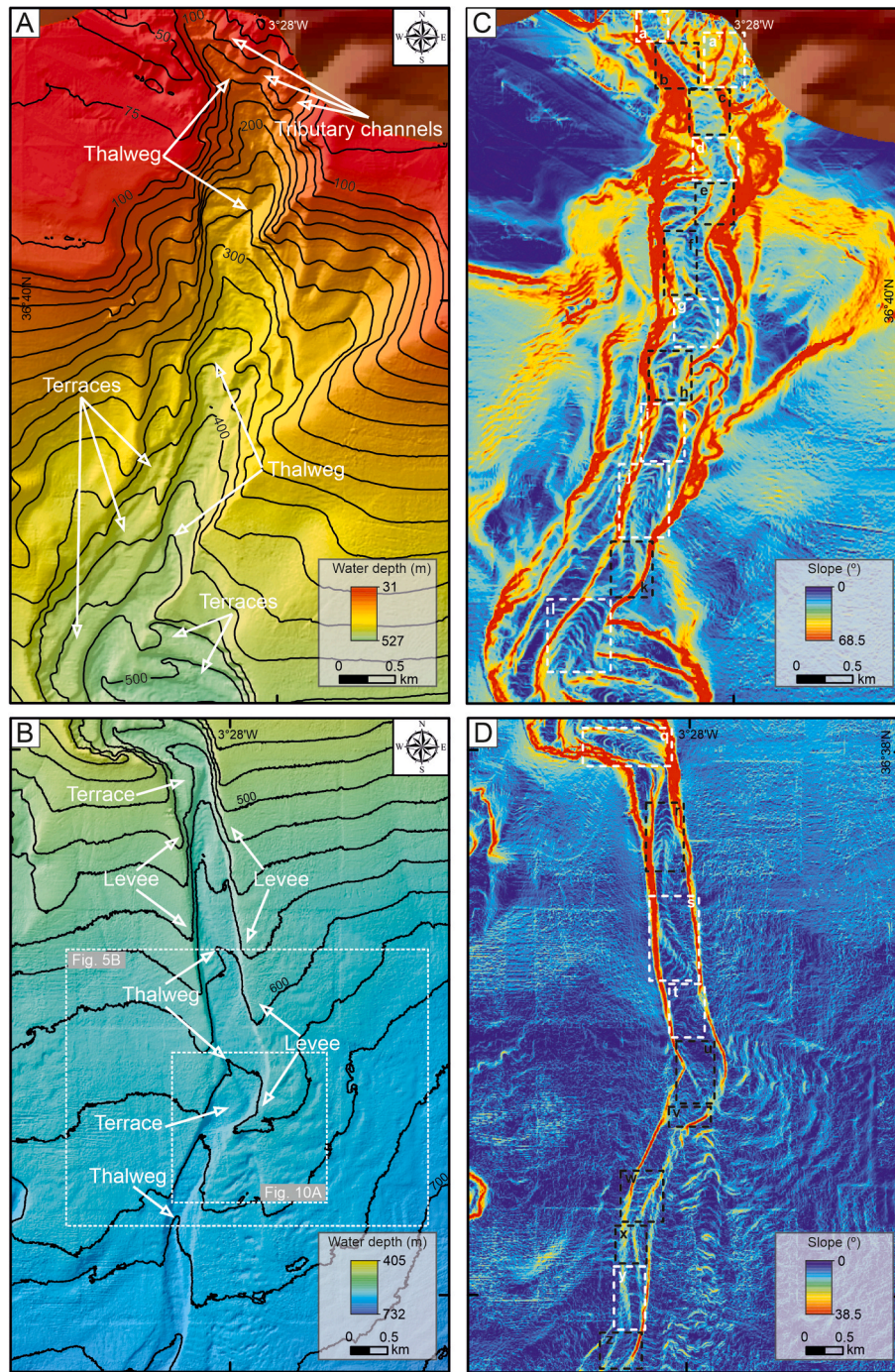
Fig. 4. High-resolution bathymetric maps of the upper (A) and the lower segments (B) of the Carchuna Canyon. Slope gradient maps of the upper (C) and the lower segments (D) of the Carchuna Canyon show the location of CSB sets according to their concavity (white rectangle: low concavity; black rectangle: high concavity). Bathymetric contours in meters. Location shown in Fig. 1C.

characterized by diffracted reflections with lateral continuity and by prominent transparent and/or chaotic layers bounded at the base by a relatively high acoustic amplitude and irregular surface.

The superficial reflections of CSBs in the axial channel are characterized by high-amplitude *acoustic facies c* (Fig. 11A, B), but they exhibit a lack of internal structure downward in the acoustic profiles (Fig. 11). In the unconfined environment located close to the bend in the lower segment of the Carchuna Canyon, scours up to 8 ms high as well as downslope sediment waves are characterized by *acoustic facies c* (Fig. 11B). Both unconfined bedforms also display a lack of internal structures downsection (Fig. 11B).

Four acoustic units were defined along the sediment wave field identified over the depositional lobe (Figs. 12 and 13). The deeper Acoustic Unit 4 exhibits *acoustic facies c* (Fig. 12) in the upper sector of the sediment wave field. Downslope in the lower sector, a lenticular-shaped body 1100 m long and with laterally variable thickness —from 14 ms to 10 ms— is identified (Fig. 13). This lenticular body is characterized by *acoustic facies c* that evolve downslope to *acoustic facies b* up to 7 ms thick (Fig. 13). Acoustic Unit 3 is characterized by *acoustic facies a* up to 5 ms thick (Figs. 12 and 13) that change downslope to *acoustic facies b* (Fig. 12).

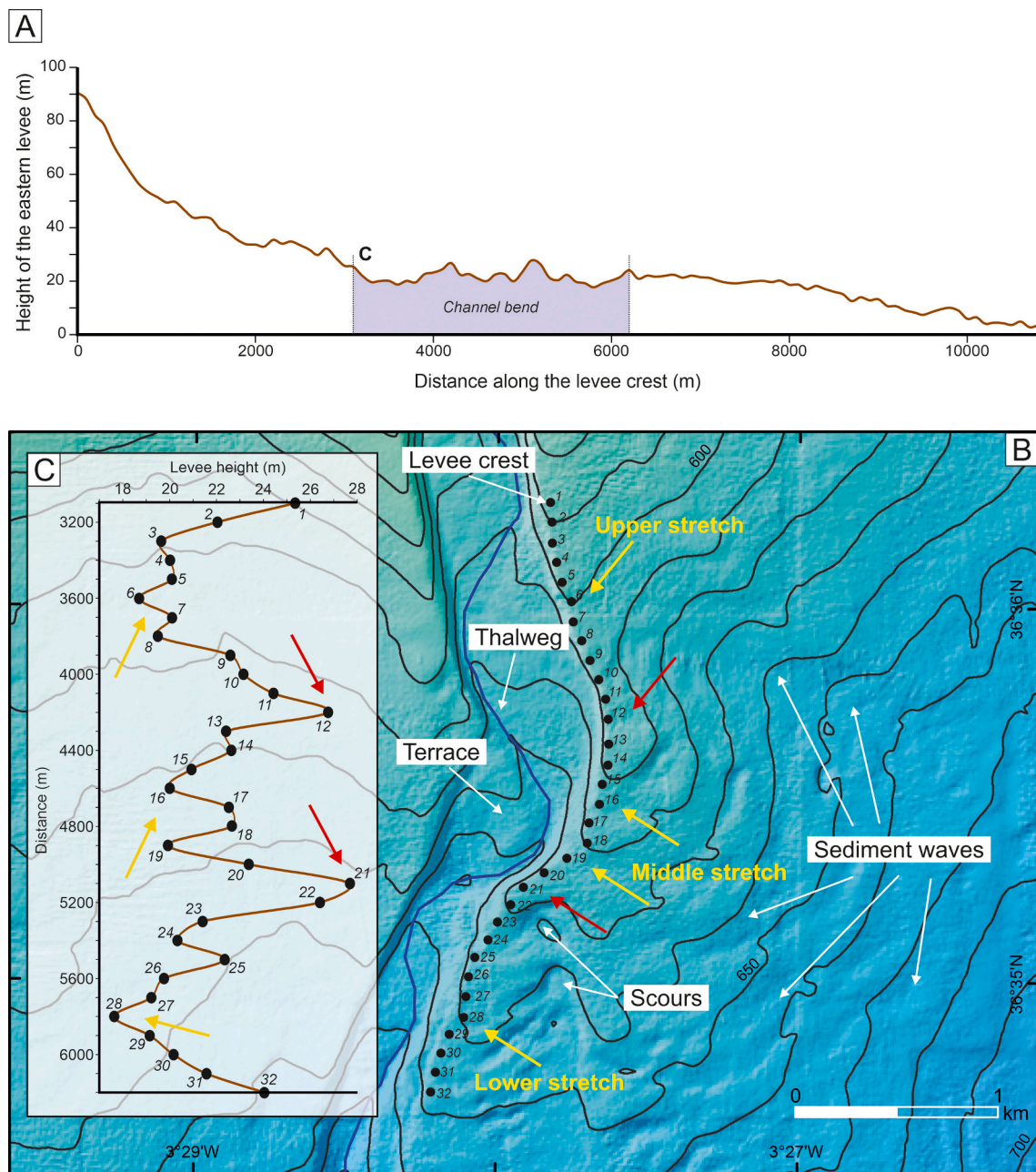Acoustic Unit 2 is characterized by *acoustic facies c* in the upper

Fig. 5. (A) Height of the eastern levee crest along the channel bend in the lower segment of the Carchuna Canyon. (B) Zoomed-in high-resolution bathymetric map of the channel bend in the lower segment, showing the points along the levee crest where the levee height was calculated (C). Red arrows mark the highest height values along the levee. Yellow arrows mark the upper, middle and lower stretches along the channel bend with the lowest height values in the levee. Bathymetric contours in meters. Location shown in Fig. 4B. (For interpretation of the references to colour in this figure legend, the reader is referred to the web version of this article.)

sector of the sediment wave field, changing to *acoustic facies d* towards the east (Fig. 12). Downslope in the lower sector, a 2–10 ms thick lenticular body is characterized by *acoustic facies c* that change downslope to *acoustic facies e* (Fig. 13). Further downslope, *acoustic facies c* up to 1 ms thick evolve seaward to *acoustic facies d*. The uppermost Acoustic Unit 1 is characterized by *acoustic facies a* up to 4 ms thick (Figs. 12 and 13), generating a wavy seafloor topography. This acoustic unit exhibits *acoustic facies c* up to 1 ms thick in the upper and lower sectors of the sediment wave field (Figs. 12 and 13).

4.3.2. Interpretation of acoustic facies

The acoustic facies identified in the study area are thought to result from distinct sedimentary processes in the unconfined setting of the Carchuna Canyon. We suggest that transparent reflections (*acoustic facies a*) are linked to low-density turbidity currents characterized by fine-grained sediments (e.g., Scacchia et al., 2022). On the other hand, high-density turbidity currents can generate either high-amplitude parallel reflections (i.e., *acoustic facies d*) (e.g., Droz et al., 2003; García et al., 2006; Sylvester et al., 2012; Li et al., 2017) or cyclic steps characterized by *acoustic facies c* (e.g., Schattner and Lazar, 2016; Wunsch et al., 2017). Downslope, parallel reflections (i.e., *acoustic facies b*) are thought to be formed by decreased flow velocities (e.g., von Lom-Keil et al., 2002). High-amplitude chaotic reflections of *acoustic facies e* are typically linked to mass-transport deposits, as suggested in numerous deep-water studies (e.g., Rogers et al., 2015; Li et al., 2017; Wang et al., 2017; Normandeau et al., 2019; Wan et al., 2022).
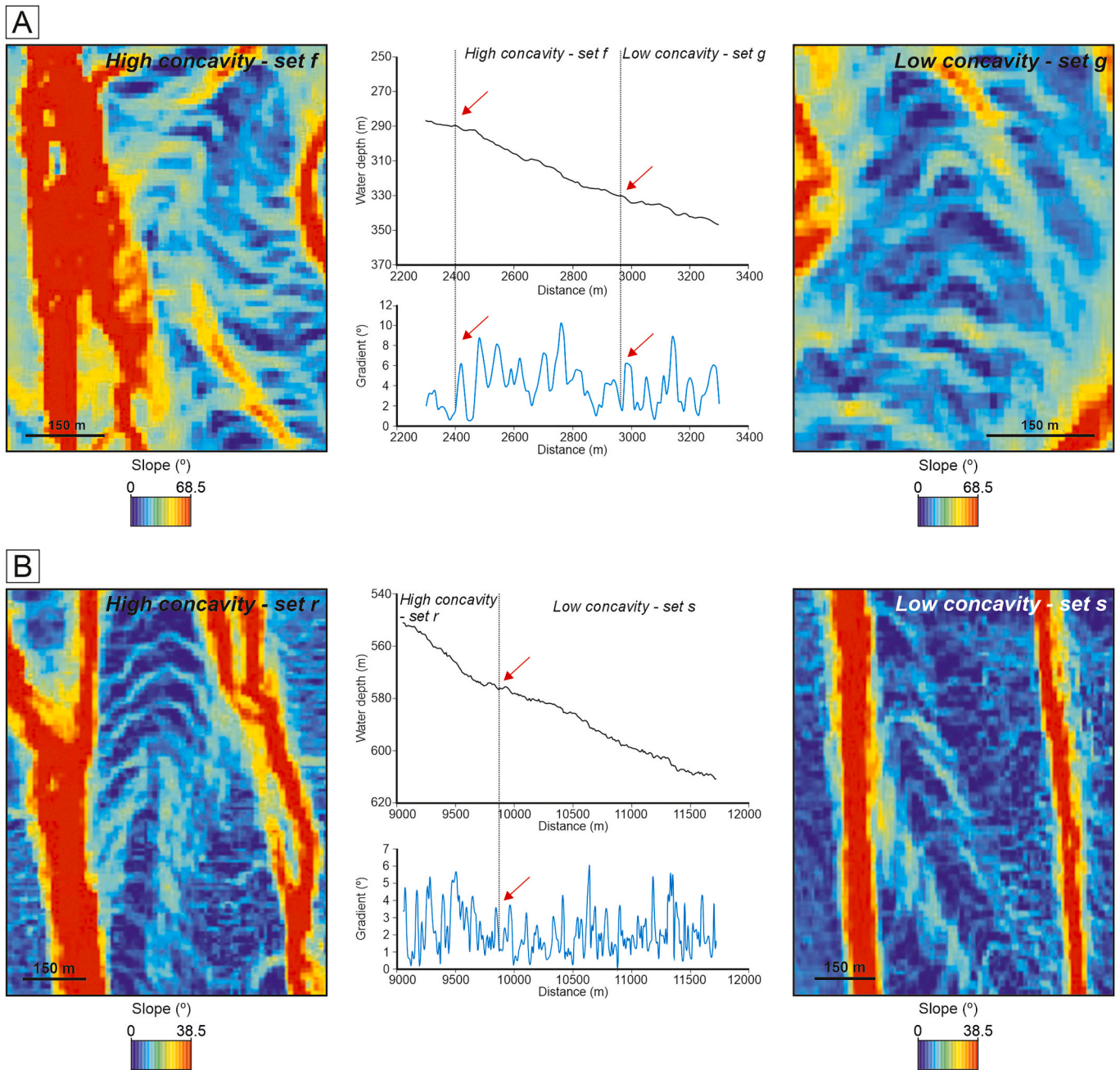
Fig. 6. Zoomed-in high-resolution bathymetric maps of the study area showing several examples of CSB sets with high and low concavity in the upper (A) and lower (B) segments. The variation from high to low concavity linked to slope gradient changes of the CSB sets is also shown. See Fig. 4C and D for location.

4.4. Sediment transport simulation

The highest simulated flow velocities are found along the Carchuna Canyon thalweg (Fig. 14A). In the upper segment, the flow follows the sinuous path of the thalweg, with the highest flow velocities between 210 and 335 m water depths. At 250 m water depth, the simulation shows maximum flow velocities. Downslope from 335 m water depth, the flow velocity decreases up to the termination of the upper segment at 500 m water depth. The lowest values of flow velocity in the upper segment occur in the lateral terraces. The highest Froude values of the flow model occur in the walls adjacent to the lateral terraces of the upper segment, whereas the lowest values occur over the terraces. The sinuous path of the thalweg is characterized by intermediate values of the Froude number (Fig. 14B).

In the lower segment, the flow follows the sinuous path of the

thalweg with the highest flow velocities between 500 and 595 m water depths (Fig. 14A). Downcanyon, the flow velocity decreases along the thalweg. Along the sinuous path of the thalweg, the simulated flow shows intermediate values of the Froude number. A spillover extending over the depositional lobe was identified at the bend in the lower segment. The simulation shows three overflow orientations: a western flow with NE-SW orientation, parallel to the main channel; an eastern flow with N-S orientation, along the main train of scours defined in the eastern overbank deposit; and an eastern flow with NW-SE orientation along the sediment wave fields (Fig. 14B). Average velocity values in the eastern overbank deposit are higher on top of the bedform crests, whereas the higher values of Froude number are located in the bedform lee sides.
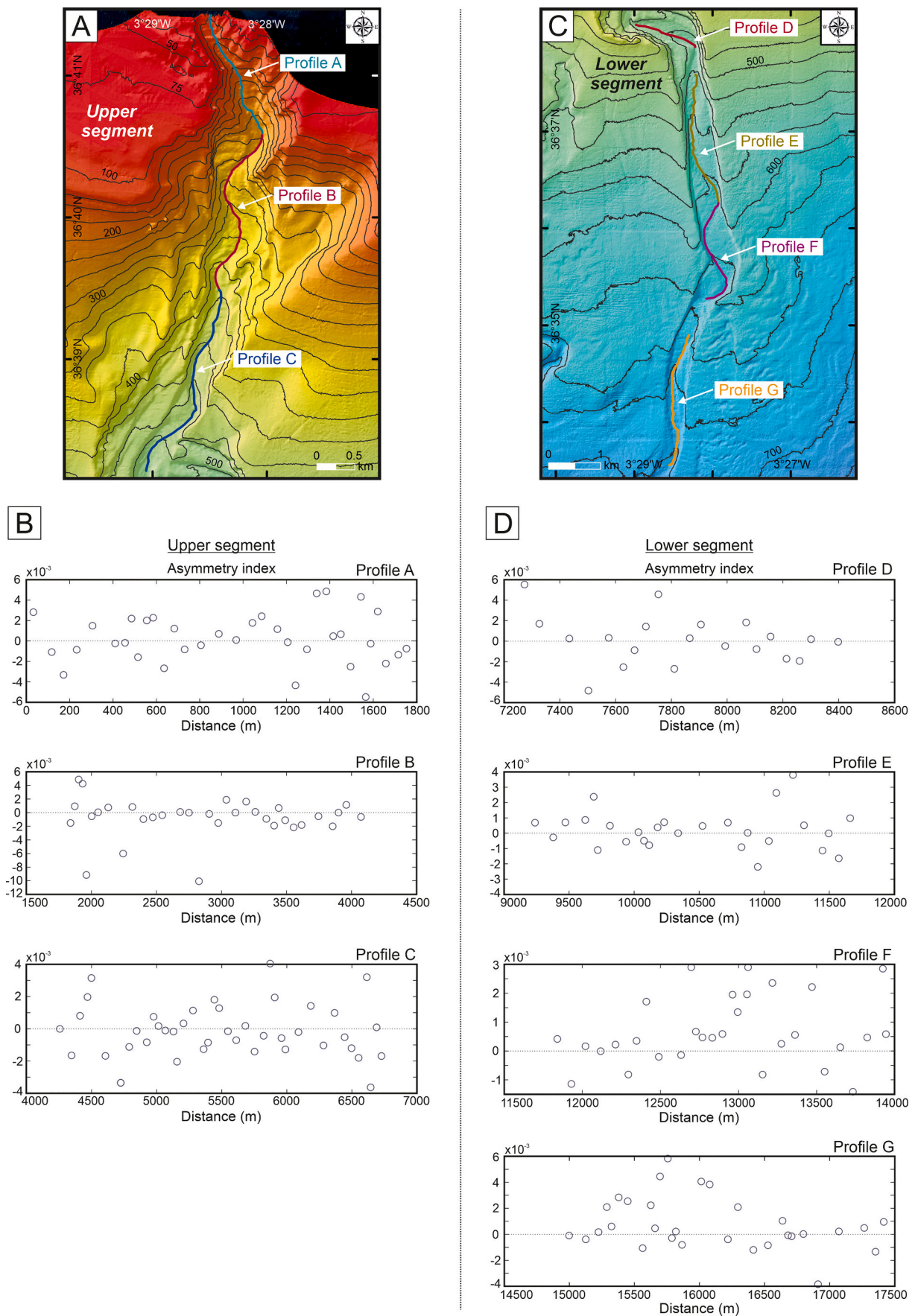
Fig. 7. Asymmetry index variability of CSBs along three longitudinal profiles (A) in the upper segment thalweg (B) and along four longitudinal profiles (C) in the lower segment thalweg (D).
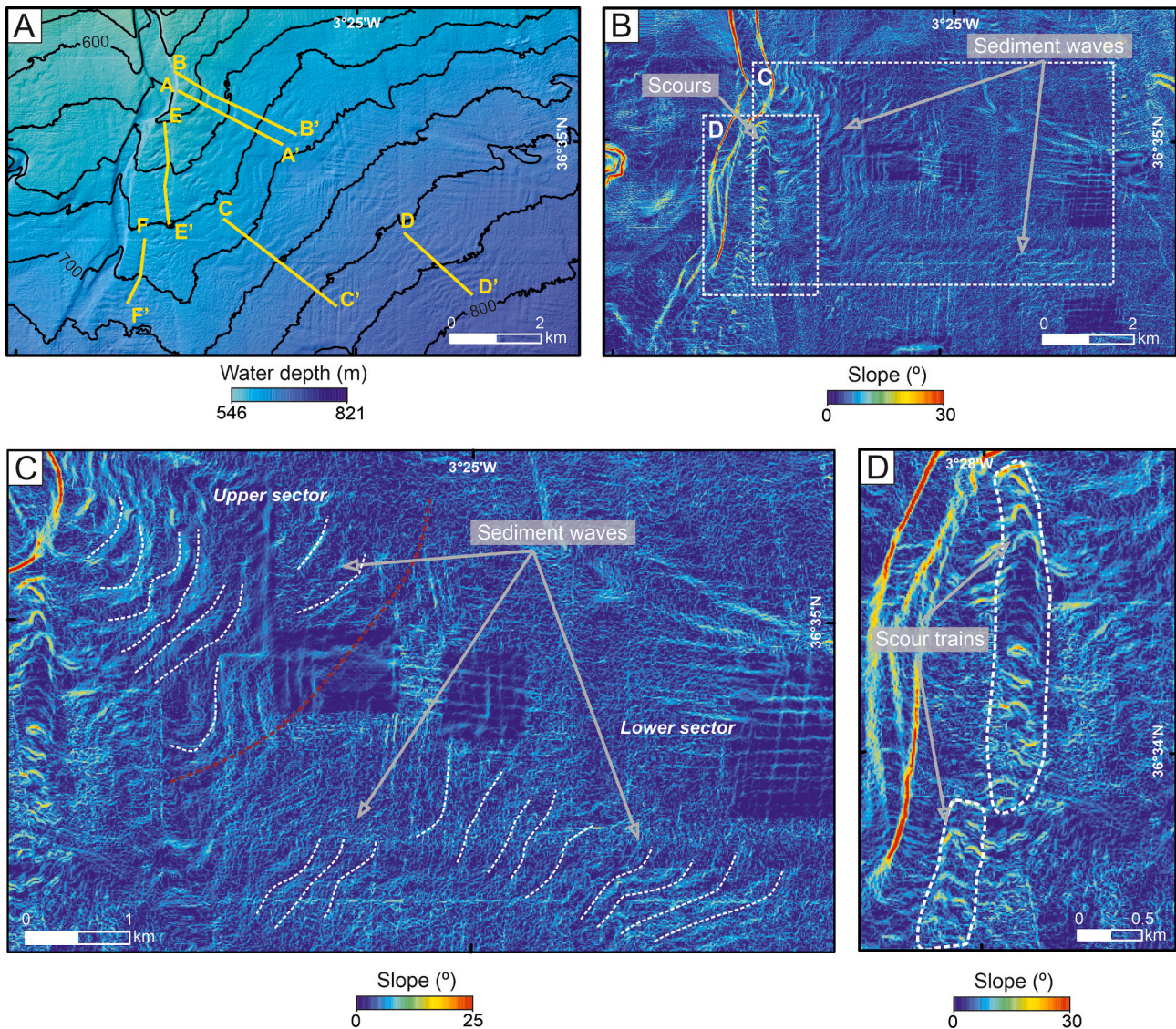
Fig. 8. (A) High-resolution bathymetric map and (B) slope map of the eastern sector of the depositional lobe of the Carchuna Canyon, with the location of bathymetric profiles shown in Supplementary material 2. (C) Zoom-in of the field of sediment waves with indication of the upper and lower sectors. (D) Zoom-in of two trains of scours identified along the depositional lobe of the Carchuna Canyon. Bathymetric contours in meters. See Fig. 1C for location.

5. Discussion

5.1. Development of cyclic steps along the confined setting of the Carchuna Canyon

5.1.1. The role of turbidity currents in CSB development

CSBs are common features in confined submarine settings mantled by coarse-grained sediments (Paull et al., 2010; Hage et al., 2018), such as the thalweg of active submarine canyons. There, CSBs are interpreted as the result of the combined effects of erosional and depositional processes during relatively short, high-energy turbidity flow events (Smith et al., 2005; Xu et al., 2008; Paull et al., 2010; Babonneau et al., 2013) that produce rhythmic seafloor bedforms known as cyclic steps (Cartigny et al., 2011; Kostic, 2011). In the Carchuna Canyon, several evidences point to the activity of confined sediment-laden gravity flows descending along the axial channel. Most notably, the presence of CSBs in the axial channel of the canyon between 95 and 706 m water depths signals the likely occurrence of flows that maintain these bedforms. This inference is supported by flow simulations that exhibit higher flow velocities along the thalweg (Fig. 14A). Additionally, very concave profiles are linked to steep and coarse-grained shelf-incised canyons in narrow

shelves adjacent to mountainous reliefs that supply coarse-grained sediments to canyon heads (Covault et al., 2011). The very concave shape and the occurrence of sandy muds and sands along the axial channel of the Carchuna Canyon (Figs. 2 and 3) would indicate a continuous supply of sandy sediments regardless of the sea-level stand and turbidity current activity throughout the channel, as documented in other canyon settings (Mitchell, 2005; Gerber et al., 2009; Kertznus and Kneller, 2009; Covault et al., 2011; Amblas et al., 2012; Cabrera et al., 2024).

Turbidity current activity is also evidenced by the CSB dimensions. CSBs in submarine canyons can be defined as *small sediment waves* (Symons et al., 2016) (Fig. 15A). These sediment waves are restricted to medium-scale canyons (<50 km) in confined settings, characterized by wavelengths from 20 to 300 m and amplitudes between 0.5 and 8 m (Symons et al., 2016), and are composed primarily of coarse-grained sediments (Paull et al., 2010). CSB dimensions in the Carchuna Canyon are consistent with their classification as *small sediment waves* (Fig. 15A), supporting CSB formation by coarse-grained turbidity current activity along the axial channel. Besides, CSBs along the axial channel of the Carchuna Canyon mostly exhibit upstream migration (Fig. 11A); in fact, they can be classified as partially erosional cyclic
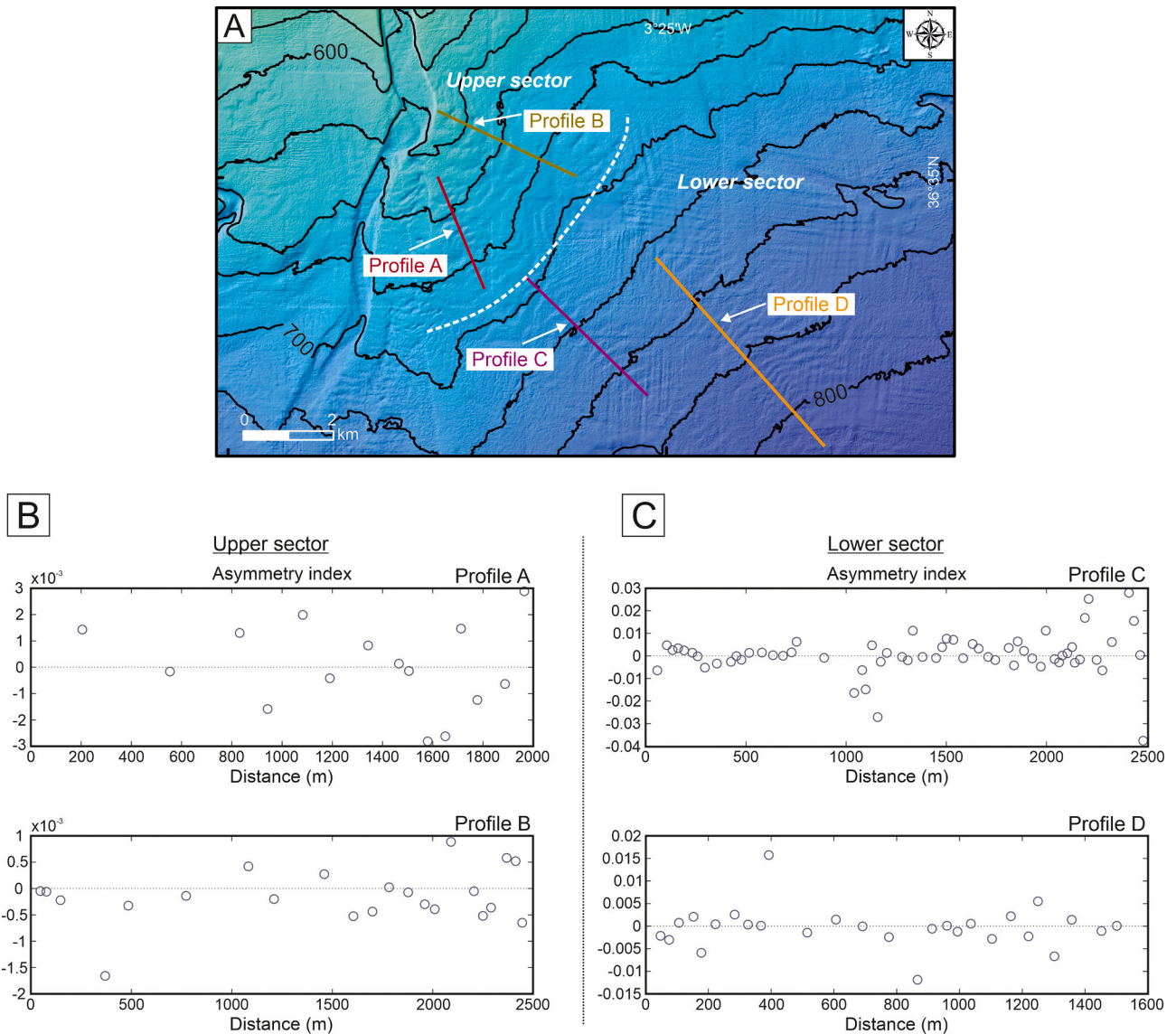
Fig. 9. Asymmetry index variability of sediment waves from two longitudinal profiles along the upper sector (A) and two longitudinal profiles along the lower sector (B) of the depositional lobe of the Carchuna Canyon.

steps (Slootman and Cartigny, 2020) due to the fact that net erosion is not limited to lee sides, but also affects the region beyond the trough on the upstream part of stoss sides. Indeed, the backsets of the CSBs at the downstream end of stoss sides are truncated by upstream-advancing lee sides (Fig. 11A) evidencing that the canyon floor is in an overall degradational state. The fact that CSBs in confined settings do not have a well-defined internal stratigraphy is linked to the erosive behavior of turbiditic flows (e.g., Paull et al., 2010; Zhong et al., 2015), which are formed by very dense, coarse-grained layers (Cartigny et al., 2013; Symons et al., 2016). In this sense, the lack of stratification within the cyclic steps along the axial channel of the Carchuna Canyon (Fig. 11) provides additional evidence of the dominance of erosion over deposition along the canyon seafloor, as documented in other canyon settings (Zhong et al., 2015).

The inferred gravity flows in Carchuna Canyon could be traced to a combination of factors, involving increased shear stresses that frequently mobilize coarse-grained sediments (Cerrillo-Escoriza et al., 2024), as in canyon heads similarly close to coastlines (Smith et al., 2018). Thus, the Carchuna Canyon head could act as a sediment trap due to its proximity to the coastline, enabling the capture of littoral cell sediments, then sediment transport along the axial channel towards the

channel termination owing to gravity flows (Cerrillo-Escoriza et al., 2024). Additionally, the proximity of the Carchuna Canyon to the coast would favor the energy concentration of coastal and storm waves, focusing in the canyon head (Ortega-Sánchez et al., 2014). These processes could erode proximal sandy infralittoral prograding wedges, providing a coarse-grained sediment source for the development of gravity flows (Cerrillo-Escoriza et al., 2024). Besides, downcanyon sediment transport pulses generating the confined cyclic steps along the axial channel can be driven by downcanyon bottom flows —postulated to occur in the Carchuna Canyon head (Serrano et al., 2020). The occurrence of such sediment transport trends is supported by the identification of marine litter at the distal termination of the channel (Cerrillo-Escoriza et al., 2023).

5.1.2. Variability in CSB geometries along the axial channel

The geometric characteristics of bedforms gradually change as the slope gradients of submarine canyon axial channels decrease downslope (Zhou et al., 2021). In axial channels, downslope-decreasing gradients tend to cause flow deceleration, leading to greater wavelengths (Cartigny et al., 2011; Slootman and Cartigny, 2020) and lesser amplitudes of the cyclic steps (Normark et al., 1980; Carter et al., 1990;
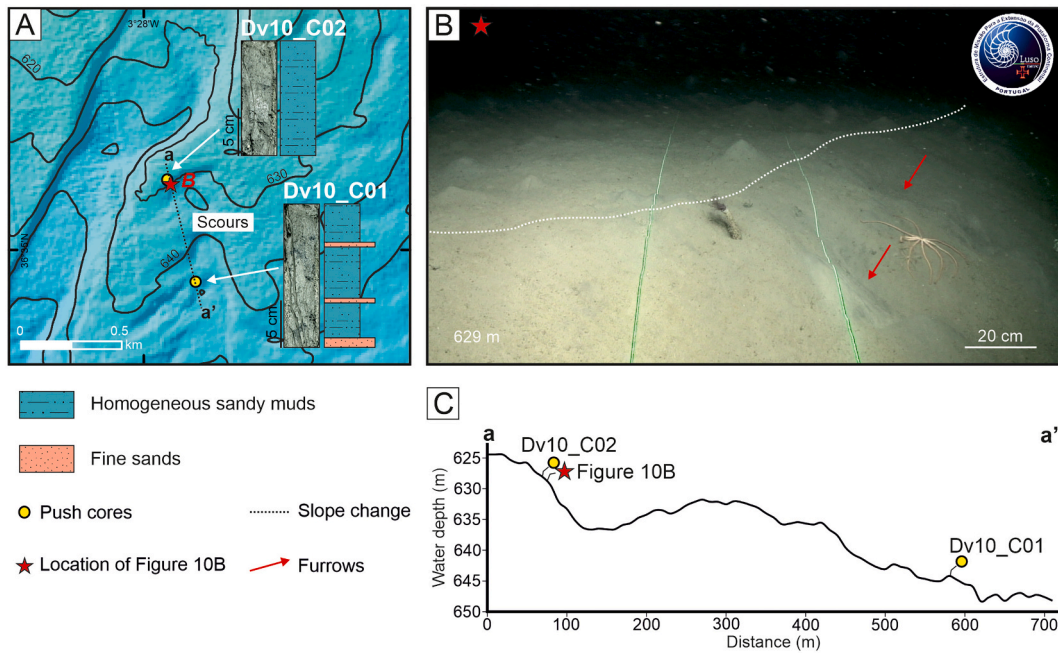
Fig. 10. (A) Zoomed-in high-resolution bathymetric map of the upper reaches of the scour train showing the sedimentary logs of two push cores collected with the ROV. Location is shown in Fig. 4B. Bathymetric contours in meters. (B) Photographic image collected by the ROV showing an abrupt change of slope gradient (white dotted line) and the furrows over the wall of the scour (red arrows). Laser beam spacing of 62 cm indicated by green lines. (C) Longitudinal bathymetric profile along the scour train. The location of both sediment cores and the photographic image are indicated. Location of bathymetric profile indicated in Fig. 10A. (For interpretation of the references to colour in this figure legend, the reader is referred to the web version of this article.)

Migeon et al., 2000). This general trend is also observed in the CSBs along the Carchuna Canyon axial channel, where the overall downslope decrease in slope gradient along the axial channel coincides with a downslope increase in cyclic step wavelength and a decrease in amplitude (Fig. 15B; Table 1). Hence, steeper slope gradients and coarser sediments in the upper segment of the Carchuna Canyon would favor the formation of shorter and higher CSBs with steeper stoss sides, in contrast to the lower segment.

Downslope asymmetries appear to characterize coarse-grained cyclic steps in confined settings (Migeon et al., 2000; Symons et al., 2016), as reported in the Monterey Canyon (Smith et al., 2005, 2007; Xu et al., 2008) and the Var Canyon (Piper and Savoye, 1993; Khripounoff et al., 2012). CSBs recognized along the upper segment of the Carchuna Canyon axial channel mostly exhibit downcanyon-directed asymmetries (Fig. 7A, B) that can be related to a high amount of sediment available for entrainment by overrunning turbidity currents (Kostic, 2011). High slope gradients in the canyon's upper segment (Fig. 3) would moreover favor the preferential development of downslope asymmetries, as is evidenced in other coarse-grained cyclic steps in confined settings (Migeon et al., 2000; Symons et al., 2016; Sun et al., 2023). In contrast, most of the CSBs in the lower segment of the Carchuna Canyon exhibit upcanyon-directed asymmetry (Fig. 7C, D) pointing to an environmental energy decrease (Cartigny et al., 2011), likely due to lower slope gradients (Fig. 3). This trend can furthermore be interpreted because the distances required for flow acceleration towards flow supercritical conditions on the stoss sides increase (Normandeau et al., 2016).

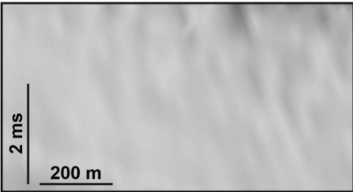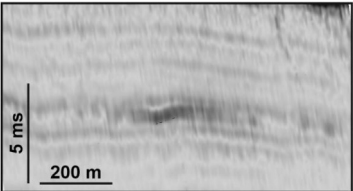*5.1.3. Implications of local variability in the slope gradient*
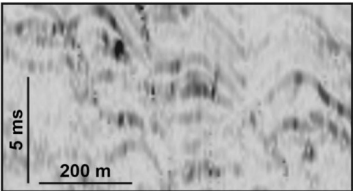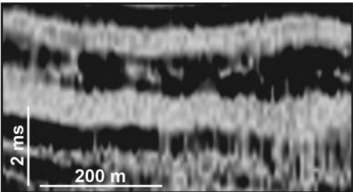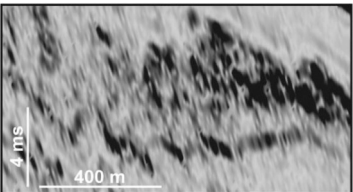
Differences in asymmetry, wavelength, amplitude, and concavity between CSB sets observed along the axial channel (Fig. 3; Table 1) could be indicative of variable flow behavior along the Carchuna Canyon path. Local variations of slope gradient affect both velocities and concentrations of bottom sediment flows; this phenomenon is consistent with variation in the behavior of turbidity currents flowing downcanyon (Kostic, 2011; Covault et al., 2017; Casalbore et al., 2018; Maselli et al., 2019; Zhou et al., 2021; Pohl et al., 2022). The increase in slope gradient

promotes the formation of hydraulic jumps (Kostic, 2011), which increase flow velocities (Wilkin et al., 2023) and support sediment erosion and bypass (Kneller and McCaffrey, 1995); as a consequence, shorter and higher cyclic steps tend to be formed (Covault et al., 2017). In contrast, decreased slope gradients facilitate a decrease in flow velocities and sediment deposition (Kneller and McCaffrey, 1995; Kubo and Nakajima, 2002).

In the axial channel of the Carchuna Canyon, we propose that bedform set dimensions and concavity are determined to a large extent by gradient changes observed along the canyon thalweg. Highly concave CSB sets have higher amplitudes and lower wavelengths (e.g., sets *b, c, e, f, r, u, v, w, x*, and *z*; Fig. 3; Table 1) that are usually related to locally increased seafloor gradients (Figs. 6 and 15C). Such local increases in slope gradients would induce flow accelerations and erosive behavior, leading to the formation of highly concave CSB sets, where the erosion rate on steeper lee sides would increase bedform amplitude (Casalbore et al., 2014; Covault et al., 2017) and decrease bedform wavelength (Covault et al., 2017; Slootman and Cartigny, 2020; Sun et al., 2023). The formation of these highly concave CSB sets may also be favored by the prevalence of coarse-grained sediments in the axial channel (Fig. 2), considering that coarse-grained cyclic steps tend to show increased heights and decreased wavelengths (Dietrich et al., 2016; Slootman and Cartigny, 2020). Following this interpretation, we infer that CSB sets with low concavity can be linked to flow decelerations leading to enhanced deposition and/or suppressed incision.

There are a few exceptions where highly concave CSB sets are not located in areas with increased seafloor gradients, but instead, occur along meanders of the Carchuna thalweg (e.g., sets *h* and *k*; Fig. 3; Table 1). We infer that these CSB sets are influenced by increases in flow density resulting in either more sediment entrainment or more erosion (Cartigny et al., 2011) along these thalweg bends. Downcanyon, these high concavity CSB sets change to low concavity sets (Fig. 3) driven by decreasing slope gradients, favoring a decrease of flow velocities. Therefore, we infer that downslope variations of CSB set concavity mainly reflect spatially variable, discontinuous axial channel flows that remobilize and concentrate sediment in a step-like fashion, triggering

Table 2
Acoustic facies defined in the acoustic profiles.

Acoustic facies	Description
Acoustic facies a	Transparent reflections.
Acoustic facies b	Continuous and parallel reflections with low to moderate amplitude.
Acoustic facies c	Undulating, discontinuous medium to high amplitude reflections.
Acoustic facies d	Parallel and gently undulating reflections with high amplitude.
Acoustic facies e	Chaotic reflections with high amplitude.

sediment transport pulses downstream.

5.2. Development of cyclic steps along the unconfined setting of the Carchuna Canyon

5.2.1. Factors that control the overflows in the Carchuna Canyon

Flow stripping can occur by spillover of the upper parts of the flows at submarine canyon meanders if the flow is thicker than the confinement height, whereas the lower part of the flow would continue moving downcanyon (Piper and Normark, 1983; Peakall et al., 2000; Fildani et al., 2006; Sumner et al., 2013; Hansen et al., 2015; Tubau et al., 2015; Covault et al., 2017). Spillover processes and increased turbulence can also be triggered by the action of centrifugal force at channel bends, which gives rise to increased flow velocity (Migeon et al., 2004; Tek et al., 2022; Scacchia et al., 2022). In the Carchuna Canyon, spillover flows can be envisaged at the bend located in the lower canyon segment. Indeed, silty sediments characterize overbank deposits at the canyon

bend, while sandy sediments can be found at the distal termination of the channel (Fig. 2). It is therefore inferred that fine-grained sediments are continuously deposited on the lateral canyon levees, whereas coarse-grained sediments are concentrated in the lower part of the flows and remain confined within the canyon, allowing the deposition of coarse sediments farther downstream.

The slope gradients of the lower segment of the Carchuna Canyon (>2°; Fig. 3) are high in comparison with other lower reaches of axial channels in shelf-incised submarine canyons (<1°; e.g., Fildani et al., 2006; Lamb et al., 2008; Zhong et al., 2015; Zhou et al., 2021). Evidences found in the Carchuna Canyon supports that these relatively high gradients could favor high flow velocities leading to downcanyon increases in sediment entrainment and flow turbulence. For example, a set of straight, high-concavity CSBs is located in the channel bend (Fig. 4). Additionally, surficial sediments over the Carchuna Canyon inner bend terrace are characterized by coarse-grained sediments (Fig. 2), suggesting that the flow is very substantial and engulfs the entire channel bend, favoring both downstream sediment transport and spillover over the levee in the channel bend, as reported elsewhere (e.g., Hansen et al., 2015).

In proximal levee areas, local flow directions of overflows are highly variable, owing to the irregular heights along the levees (Normark et al., 2002; Migeon et al., 2004; Hansen et al., 2015; Tek et al., 2022). Although the studied bedforms are essentially concentric around the channel bend of the Carchuna Canyon, a spatial relationship is established between the development of bedform fields over the overbank deposit and lowered levee heights in the proximal areas of the bedform fields (i.e., upper, middle, and lower levee stretches; Fig. 5). We infer that these depressed levee stretches are genetically linked with overflow paths that generate sediment waves (Fig. 16A). Considering that the minimum levee height in the channel bend is 17.5 m, we speculate that turbidity currents descending along the axial channel and approaching the channel bend most likely exhibit thickness around that value or just slightly less, given that channel bends induce flow acceleration as a result of centrifugal force, and favor flow stripping (Migeon et al., 2004).

In contrast to the relationship found between sediment wave fields and lowered levee stretches, the scour trains found in the overbank deposit of the Carchuna Canyon are not related proximally with low levee heights (Fig. 5). In this case, we surmise that the drastic change of orientation of the axial channel in the lower segment (NNW-SSE to NNE-SSW; Figs. 2 and 5) would be a key factor in the formation of the scours. In other sharp bends of submarine canyons, turbidity currents tend to flow downslope of orientation changes by overflowing the levee crests (e.g., Fildani et al., 2006). We infer that the studied scour trains formed by means of a mechanism similarly described at channel bends (e.g., Fildani et al., 2006; Covault et al., 2014); accordingly, the overflow of turbidity currents that descend along the axial channel and exceed the high levee crest at the channel bend would trigger an abrupt change in the turbidity current behavior (Fig. 16B).

5.2.2. Sediment waves formed in the overbank deposit of the Carchuna Canyon

In unconfined settings, sediment waves have been interpreted as supercritical flow bedforms, that is, net-depositional cyclic steps (Fildani et al., 2006; Cartigny et al., 2011, 2014; Kostic, 2011, 2014; Zhong et al., 2015) mantled by fine-grained sediments (Symons et al., 2016) particularly covering the overbank areas of submarine canyons and channels (Fildani et al., 2006, 2013; Kostic and Parker, 2006; Maier et al., 2011, 2013; Armitage et al., 2012; Zhong et al., 2015). The unconfined setting makes these cyclic steps more prone to form positive reliefs due to preferential sediment deposition on the upstream side (Flood and Giosan, 2002), in contrast to confined CSBs, where erosion is thought to play a larger role (Symons et al., 2016).

Because sediment waves in unconfined settings exhibit higher amplitudes and wavelengths than those found in confined canyon settings, they are categorized as *large sediment waves* (Symons et al., 2016)
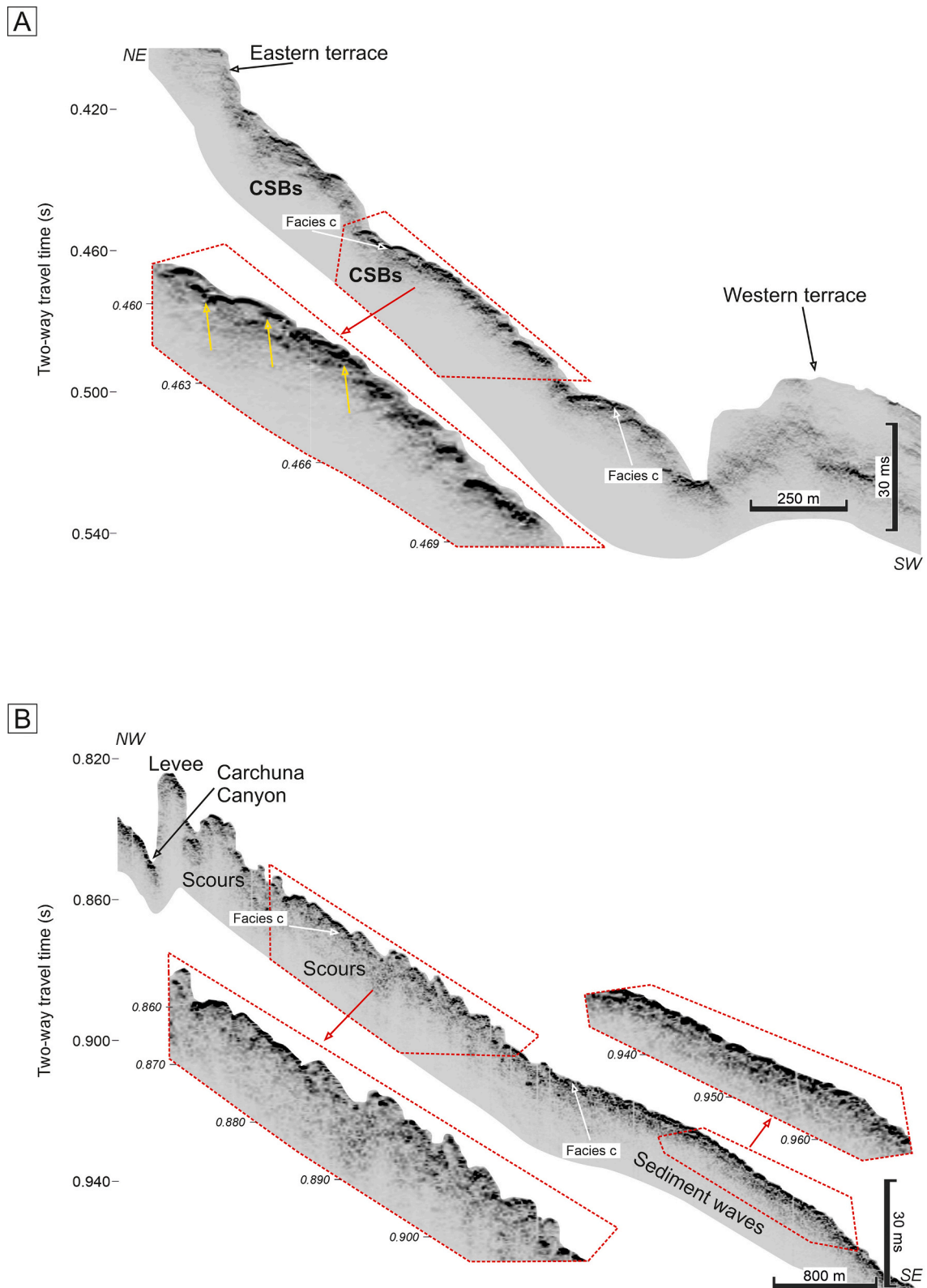
Fig. 11. (A) Acoustic profile located in the upper segment of the Carchuna Canyon, illustrating CSBs *acoustic facies c* and the lateral terraces. Zoom-in of a sector of the axial channel showing the backsets of CSBs on the downstream end of stoss sides truncated by upstream-advancing lee sides indicated by yellow arrows. (B) Acoustic profile located in the transition from the Carchuna Canyon towards the depositional lobe illustrating the scour *acoustic facies c*. Note the downslope change to sediment waves. Zoom-ins of a sector of scours and sediment waves, respectively. See Fig. 1C for location. (For interpretation of the references to colour in this figure legend, the reader is referred to the web version of this article.)
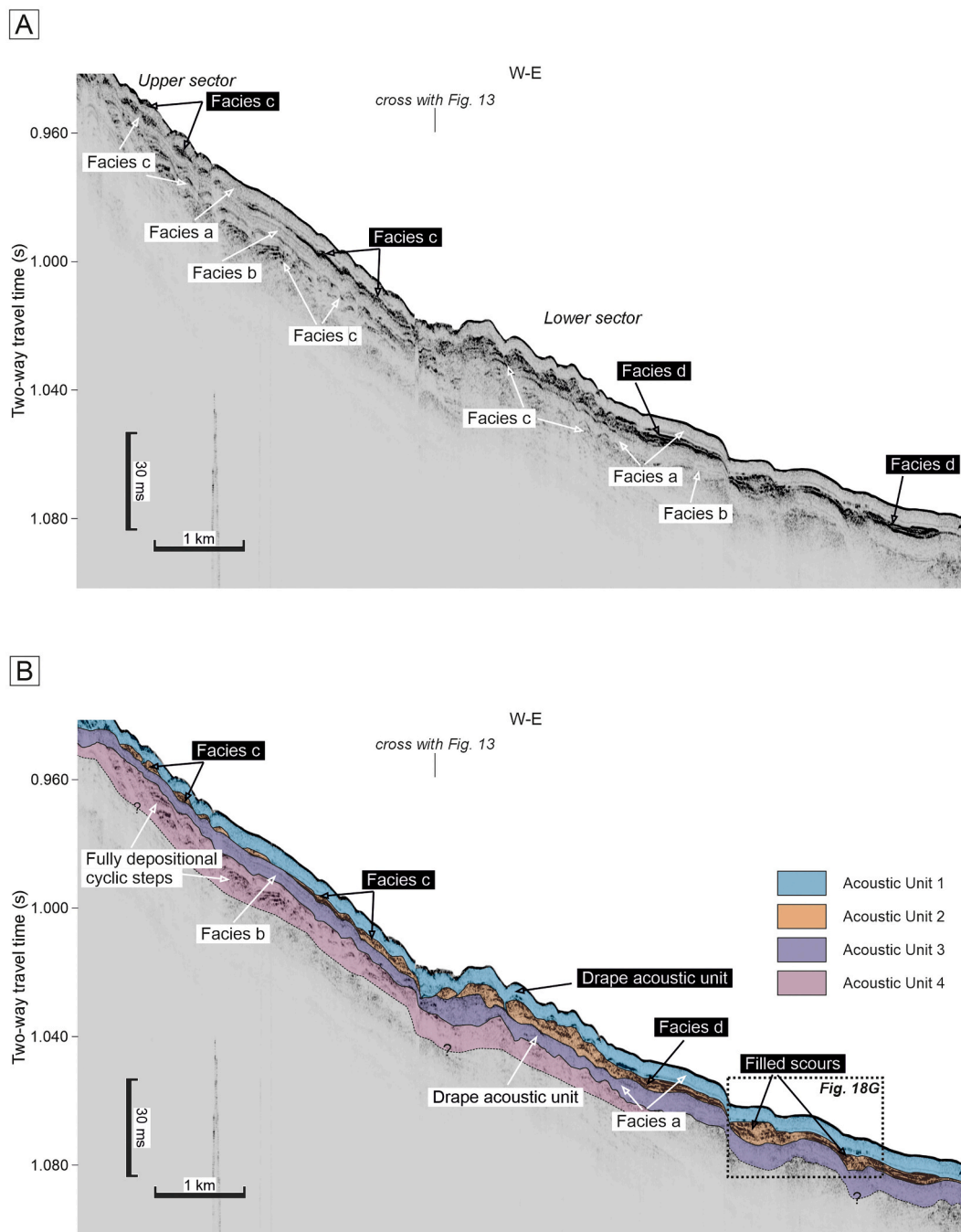
Fig. 12. (A) East-West oriented acoustic profile located in the eastern overbank deposit of the Carchuna depositional lobe with indication of acoustic facies, and (B) the interpretation of four acoustic units. Location of Fig. 18G is also indicated. See Fig. 1C for profile location.

(Fig. 15A). Amplitude and wavelength values of the unconfined sediment waves in the depositional lobe of Carchuna Canyon are larger than the CSB dimension values; hence they lie between *small* and *large sediment waves* (Fig. 15A). This fact supports a sediment wave genesis of the Carchuna depositional lobe related to the activity of fine-grained turbidity currents, in view of the genetic conditions behind *small* and *large sediment waves* put forth by Symons et al. (2016).

The crests of these unconfined sediment waves are not aligned parallel to the canyon axis (ca. NW-SE orientation of the crests vs ca. N-S orientation of the canyon axis; Figs. 8 and 16A). In addition, the flow simulation shows that the Froude number is higher on the bedform lee sides (Fig. 14B), indicating supercritical flow conditions (Cartigny et al., 2011). Both evidences point to the development of the studied sediment

waves in a context of recurring stripped turbidity currents spilling out of the axial channel (Fig. 16A), as evidenced in similar environments (e.g., Lewis and Pantin, 2002; Normark et al., 2002; Wynn and Stow, 2002; Fildani et al., 2006; Kostic et al., 2010; Covault et al., 2017). As in axial channels, decreasing slope gradients in overbank deposits cause a streamwise flow deceleration (e.g., Cartigny et al., 2011). In the overbank deposit of the Carchuna Canyon, this is evidenced by a downslope wavelength increase and amplitude decrease of the sediment waves, accompanied by a downslope decrease in flow velocities (Fig. 14A).

Upslope-directed asymmetries of cyclic steps are characteristic of fine-grained sediment waves in unconfined, low-energy environments, as at the Monterey Fan (Normark et al., 1980, 2002; Fildani et al., 2006), the Var Sedimentary Ridge (Migeon et al., 2000, 2001), the overbank
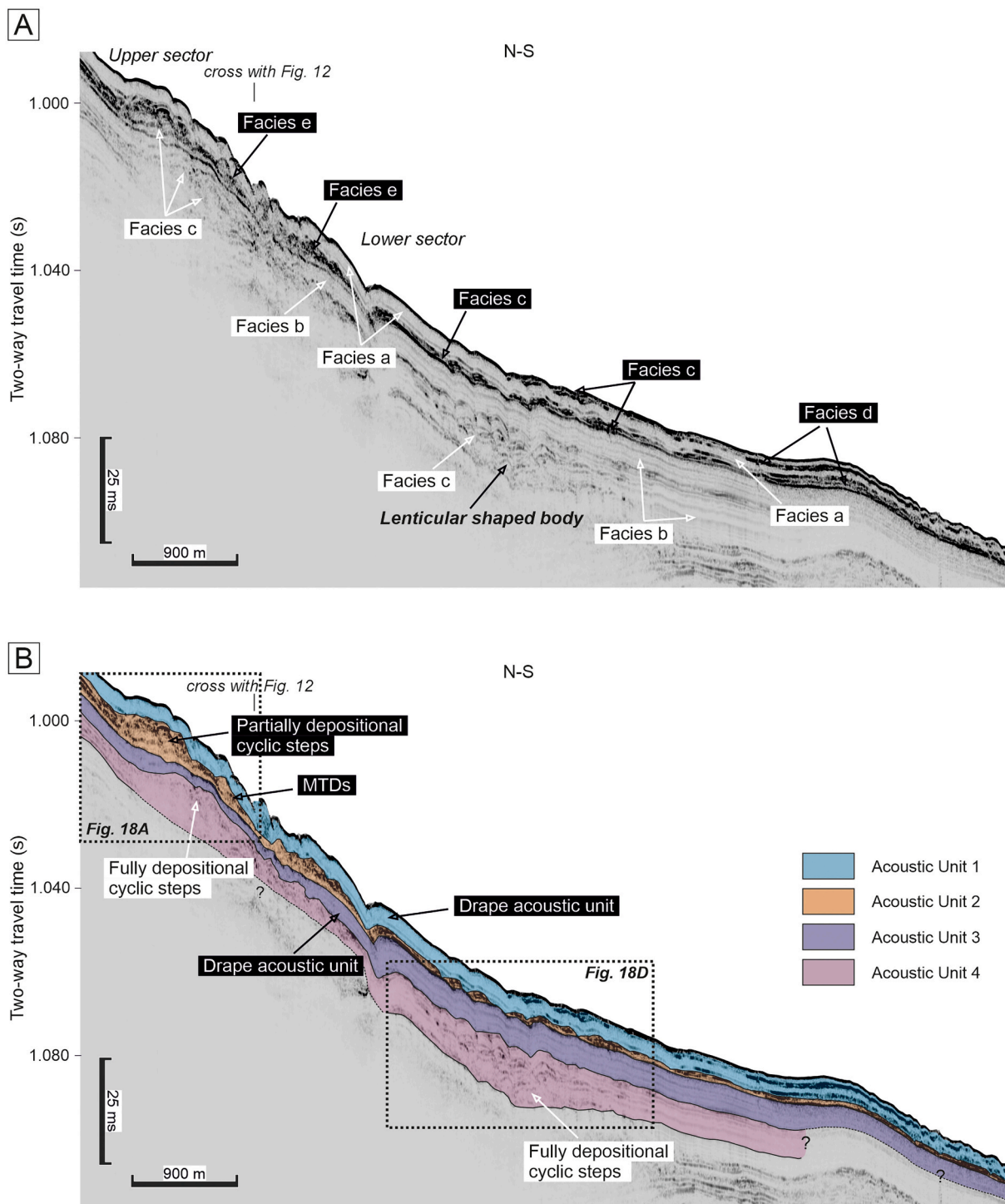
Fig. 13. (A) North-South oriented acoustic profile located in the eastern overbank deposit of the Carchuna depositional lobe with indication of acoustic facies, and (B) the interpretation of four acoustic units. Location of Fig. 18A and D is also indicated. See Fig. 1C for location.

deposits of the Eel Canyon (Lamb et al., 2008), or the overbank deposits in the Gioia Basin (Gamberi et al., 2013). However, downslope-directed asymmetries or symmetric trends of sediment waves are related to aggradational building of levees that tend to be covered by coarse-grained sediments (Kostic, 2011). Such evidence is seen in the upper sector of the overbank deposit of the Carchuna Canyon, where the coarsest-grained sediments are located close to the levee crest (Fig. 2), with sediment waves showing dominantly downslope-directed asymmetries (Fig. 9B). In contrast, the sediment waves in the lower sector over the overbank deposit exhibit an upslope asymmetry trend (Fig. 9C), suggesting that

up-slope migration dominates over vertical aggradation (Figs. 11B, 12, and 13) in relation to the distal decrease in slope gradients.

5.2.3. Scours formed in the overbank deposit of the Carchuna Canyon

Turbidity currents that mostly carry coarse-grained sediments can create large-scale scours nearby internal hydraulic jumps (Hiscott et al., 2013; Sumner et al., 2013; Covault et al., 2017). Linear trains of scours can be interpreted as a result of net-erosional cyclic steps in supercritical flows (Fildani et al., 2006; Kostic, 2011; Covault et al., 2017), where repeated hydraulic jumps along the scour trains form due to lee side
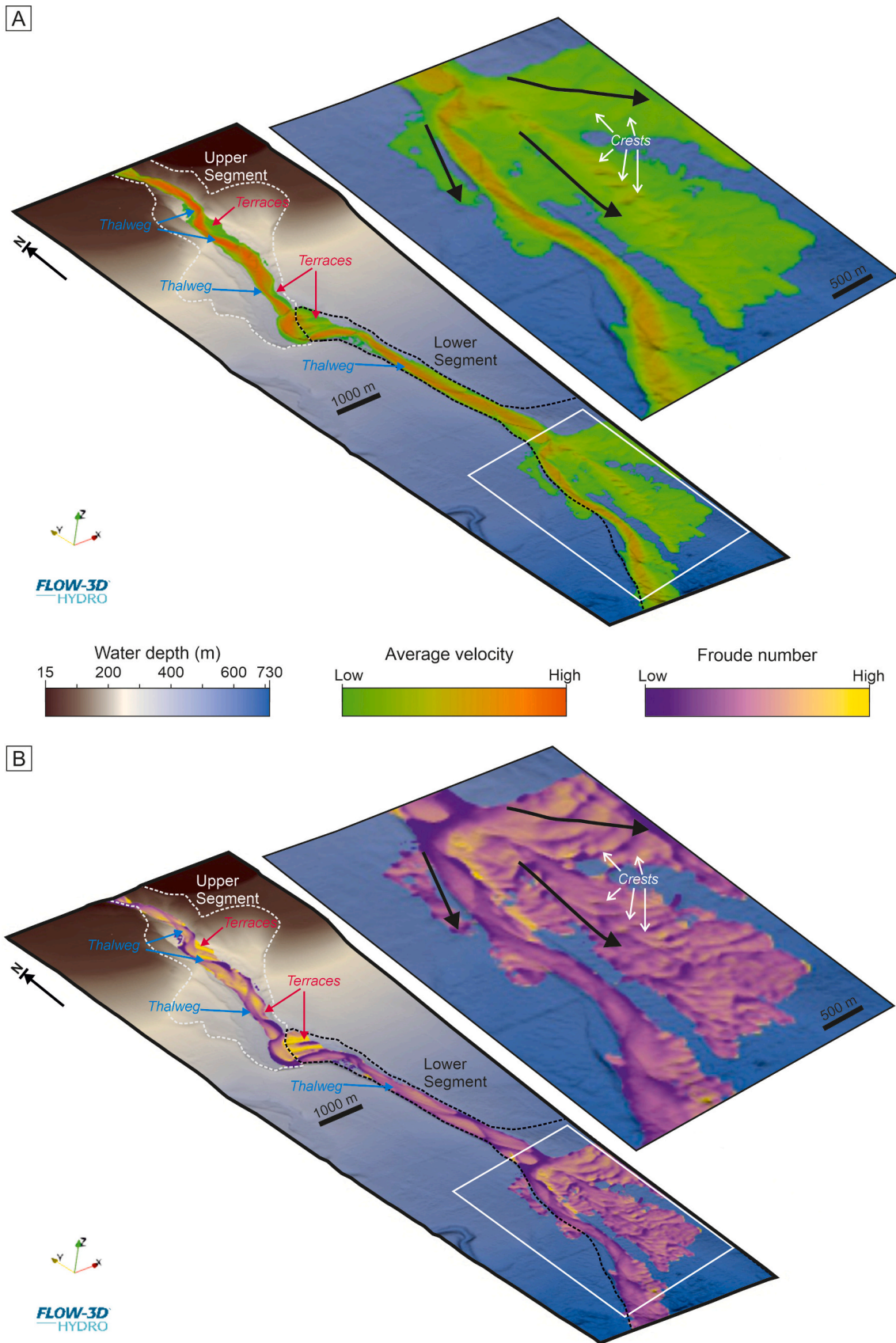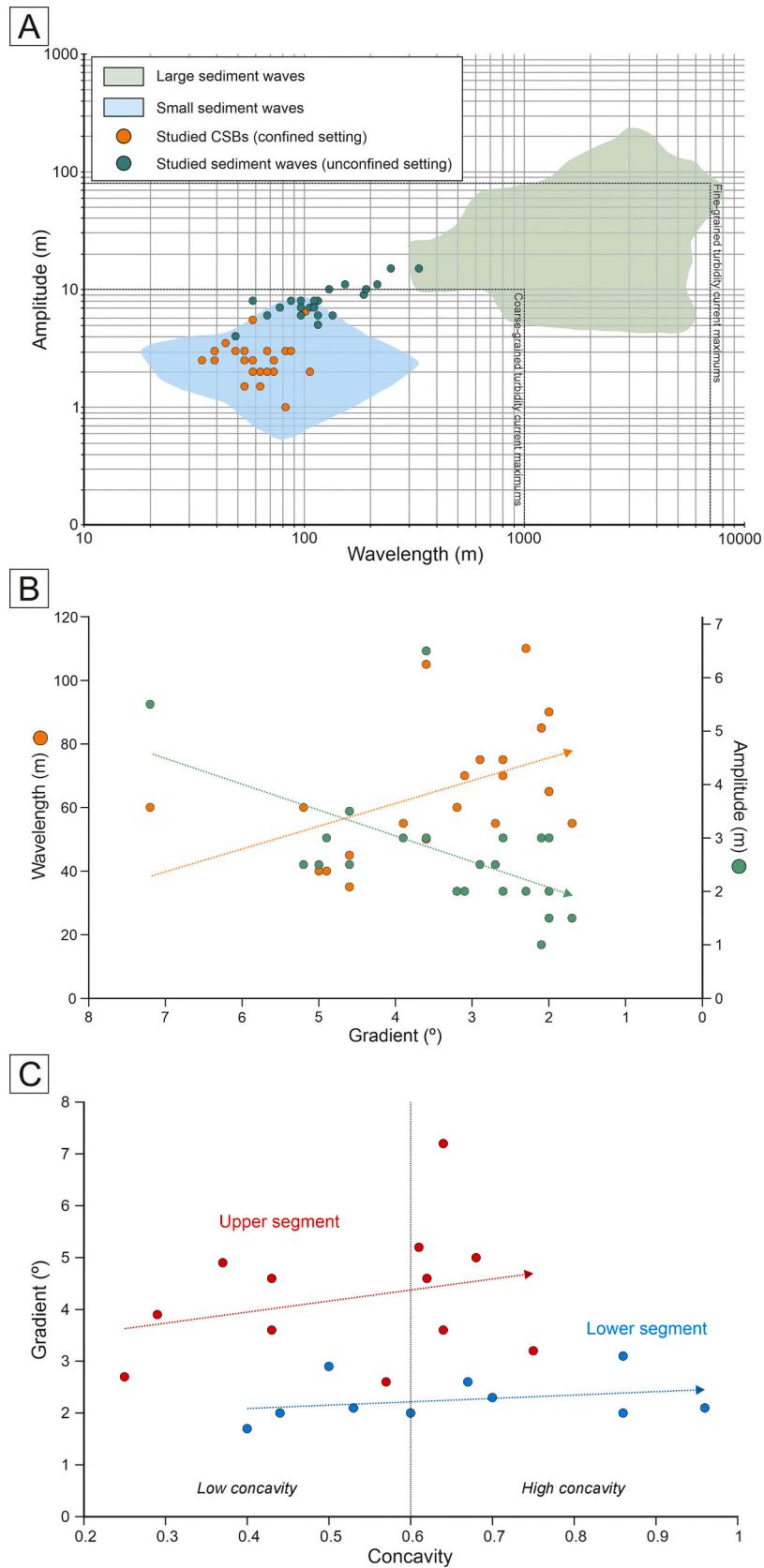
Fig. 14. Variation of the average velocity (A) and the Froude number (B) of the three-dimensional flow simulation executed along the axial channel of the Carchuna Canyon. The most significant feature is a flow spillover at the channel bend over the depositional lobe in the lower segment.

(caption on next page)

Fig. 15. (A) Logarithmic plot of wavelength versus amplitude for global bedform examples highlighting groups based on bedform scale and relief according to Symons et al. (2016). Average amplitude and wavelength values of the studied confined (orange circles) and unconfined (green circles) bedforms are plotted. The maximum wavelength and amplitude values that define the coarse- and fine-grained turbidity current boundaries are shown as dotted lines after Wynn et al. (2002). (B) Bi-variate relationships between CSB wavelengths (orange) and amplitudes (green) and the slope gradient along the Carchuna Canyon indicating the trend of each parameter with dotted arrows. (C) Bi-variate relationships between slope gradients and CSB concavity along the upper (red) and lower (blue) segments of the Carchuna Canyon, indicating the trend of each segment with dotted arrows. (For interpretation of the references to colour in this figure legend, the reader is referred to the web version of this article.)

erosion rates by Froude-supercritical flows —exceeding stoss side erosion rates by Froude-subcritical flows— ultimately causing an upstream migration (Sumner et al., 2013; Hiscott et al., 2013). Alternatively, scour trains may signal an excavation of initial bed defects by a subcritical flow with enough shear stress (Symons et al., 2016).

According to the flow model, the highest velocity values occur along the scour trains in the overbank deposit of the Carchuna Canyon (Fig. 14A). In addition, there are high values of Froude number on the lee side of scours (Fig. 14B), evidencing supercritical flows with high velocities that favor erosion on both lee and stoss sides (Slootman and Cartigny, 2020) and lead to upstream migration (Fig. 16C, D). Downslope of the scour trains, net-erosional cyclic steps evolve to net-depositional cyclic steps (Figs. 11A and 16C), thus indicating a progressive downslope decrease in sediment transport capacity and erosive flow behavior, reflected by decreasing velocities in the flow model (Fig. 14A); this pattern has been observed elsewhere (e.g., Li and Gong, 2018). Therefore, we interpret the scours located close to the bend of the Carchuna Canyon as net-erosional cyclic steps carved by flow-stripped turbidity currents that have incised the overbank deposit of the canyon (Fig. 16B, C).

The noteworthy location of the scours in the overbank deposit of the Carchuna Canyon agrees with a scenario of focused turbidity currents (e. g., Izumi, 2004) (Fig. 16B) where erosion rates are intensified in places of flow concentration, leading to channel formation in topographic lows of outer levees (Fildani et al., 2006; Normandeau et al., 2019; Maier et al., 2020). Accordingly, the scour trains studied here could mark an early phase of the Carchuna Canyon channel evolution due to an ongoing avulsion process. The flow concentration is evidenced by the distribution of surficial sediments along the scours generated in the overbank deposit of the Carchuna Canyon, the coarser sediments being found on stoss sides (Fig. 10A). This pattern may be attributed to coarse-grained sediment preferentially bypassed on the lee sides —favored by the concentration and high velocities of the overspilling flow— and deposited on the stoss sides of the following scour downslope. The erosive behavior of the flow is further evidenced over the lee side as erosive features (Fig. 10B). In contrast, finer-grained sediments are deposited upstream over the lee sides (Fig. 10A) in response to low velocities of the tails of overspilling flows, as seen in other cyclic steps on overbank deposits (e.g., Tek et al., 2022). We infer that the flow concentration in the channel bend is due to episodic, energetic sediment transport pulses that exceed the levee crest where the channel bend changes its orientation.

5.3. Recent evolution of the Carchuna Canyon

The flow density and turbulence of overspilling confined flows control the grain size partitioning between in-channel flow and levee deposits (Hiscott et al., 1997; Peakall et al., 2000; Posamentier and Walker, 2006; Scacchia et al., 2022), defining two end-member situations: low- and high-density turbidity currents (Lowe, 1982; Kneller and Buckee, 2000). In low-density turbidity currents, partial inertia-driven flow spillover may occur on outer channel bends, where fine-grained sediments in the upper part of the current escape the channel, yet the denser lower part remains within the channel (Piper and Normark, 1983; Leeder, 1999; Peakall et al., 2000; Hansen et al., 2015). In contrast, high-density turbidity currents feature heights greater than the channel confinement depth, meaning widespread coarse-grained spillover on both outer and inner channel bends (Hesse, 1995; Peakall et al.,

2000; Hansen et al., 2015).

The acoustic units that define the overbank deposit of the Carchuna Canyon suggest the occurrence of recurrent spillovers in the recent past. However, the vertical alternation of acoustic units suggests that overflows over the depositional lobe reflect different characteristics and energy conditions. Depending on the development of high- or low-density turbidity currents descending along the axial channel and approaching the sharp bend in the Carchuna Canyon (Fig. 17A), spillover processes along the channel bend and subsequent deposition in the overbank area would have been different, ultimately leading to the construction of the Carchuna depositional lobe (Fig. 17).

5.3.1. High-density turbidity current scenario

High-reflectivity acoustic facies in overbank deposits usually indicate coarse-grained sediments derived from high-density turbidity currents that generate an overall positive topography (e.g., Scacchia et al., 2022). The depositional lobe of the Carchuna Canyon contains two acoustic units (4 and 2) mainly characterized by high-reflectivity acoustic facies (Figs. 12 and 13), a likely result of high-density turbidity currents. Ample evidence supports this inference. High-amplitude reflectors that separate acoustic units have been identified in overbank deposits as abrupt sedimentological changes traced to an erosive flow behavior (Heiniö and Davies, 2009; Gong et al., 2012; Schattner and Lazar, 2016). In the Carchuna depositional lobe, the high-amplitude reflectors that limit the bases of acoustic units 4 and 2 (Figs. 12 and 13) exhibit irregular shapes that can be related to bypass processes generating local unconformities, and favoring hydraulic jumps, with the subsequent downslope increase in overflow turbulence (Fig. 18), as evidenced in other canyon depositional lobes (e.g., Li and Gong, 2018). Deposits resulting from high-density turbidity currents exhibit a spatial variability from upper to lower reaches of depositional lobes as the turbidity currents become less energetic with distance. In this sense, the imprint of high-density turbidity currents is also evidenced by the downslope increase in deposit thickness (Fig. 12) suggesting an efficient downslope sediment transfer along the depositional lobe.

Sediment wave fields exhibit different dimensions, geometries and sediment distribution, depending on the interaction between overspilling turbidity currents and slope topography (Migeon et al., 2000; Kubo and Nakajima, 2002; Cartigny et al., 2011; Maselli et al., 2019; Scacchia et al., 2022). The upper sector of the Carchuna depositional lobe hosts partially depositional sediment waves (Figs. 13, 18B) that are interpreted as low-aggradational cyclic steps indicative of coarse grained-sediments and high seafloor shear stresses (Normark et al., 2002; Kostic, 2014; Slootman and Cartigny, 2020). These bedforms can be related with highly turbulent flows capable of eroding lee sides while depositing on stoss sides. The accumulation of these sediment waves conforms a lenticular-shaped body truncated downslope (Fig. 13) that change to a MTD (Fig. 18C). This downslope variation represents a localized instability of this lenticular body as a consequence of the high accumulation of overlapping sediment waves and the high slope gradient exhibited by the proximal sector of Carchuna Canyon's sediment wave field. Instability during channel-levee building has been identified in the upper reaches of other overbank deposits in submarine canyon environments (e.g., Marsset et al., 2022).

The middle reaches of the Carchuna depositional lobe are characterized by fully depositional sediment waves (Figs. 13 and 18E), which signal a loss of erosional capacity, an aggradational state, and high
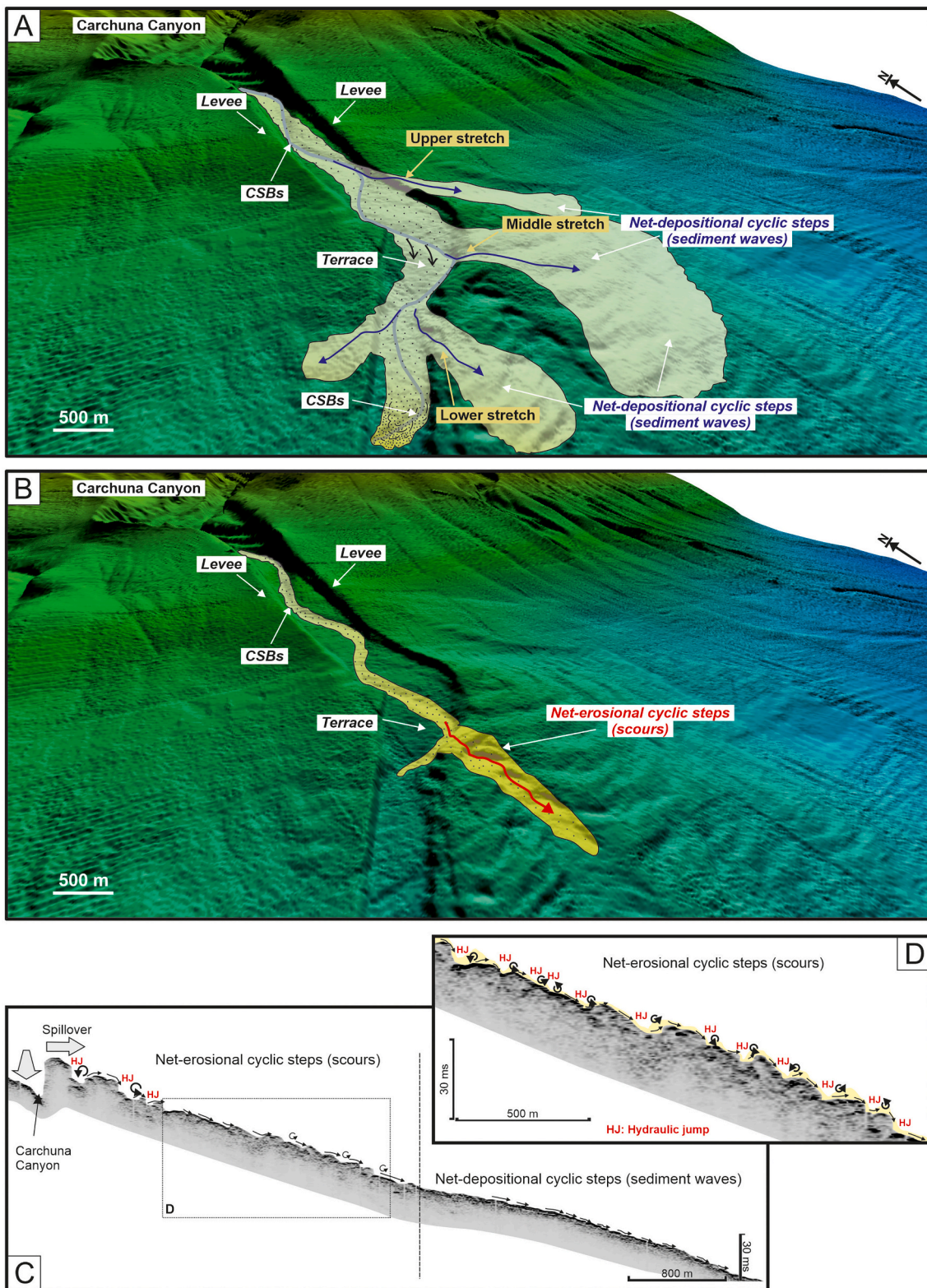
Fig. 16. 3D reconstruction of the study area illustrating two different settings according to development of bedforms along the overbank deposit at the channel bend of the Carchuna Canyon. (A) Three main overflows (in blue) transiting along three depressed levee crests (upper, middle, and lower levee stretches) and contributing to development of sediment waves. (B) An energetic and casual turbidity flow exceeding the levee crest at the channel bend (in red) favors the erosion of the overbank deposit forming scour trains. (C) Interpretation of the acoustic profile of Fig. 11B, located from the Carchuna Canyon towards the depositional lobe, illustrating the erosional stripped flow over the scour train that evolves downslope to sediment waves. (D) Zoom-in of the upper sector of the depositional lobe illustrating the hydraulic jumps of the flow along the scour train (net-erosional cyclic steps). (For interpretation of the references to colour in this figure legend, the reader is referred to the web version of this article.)
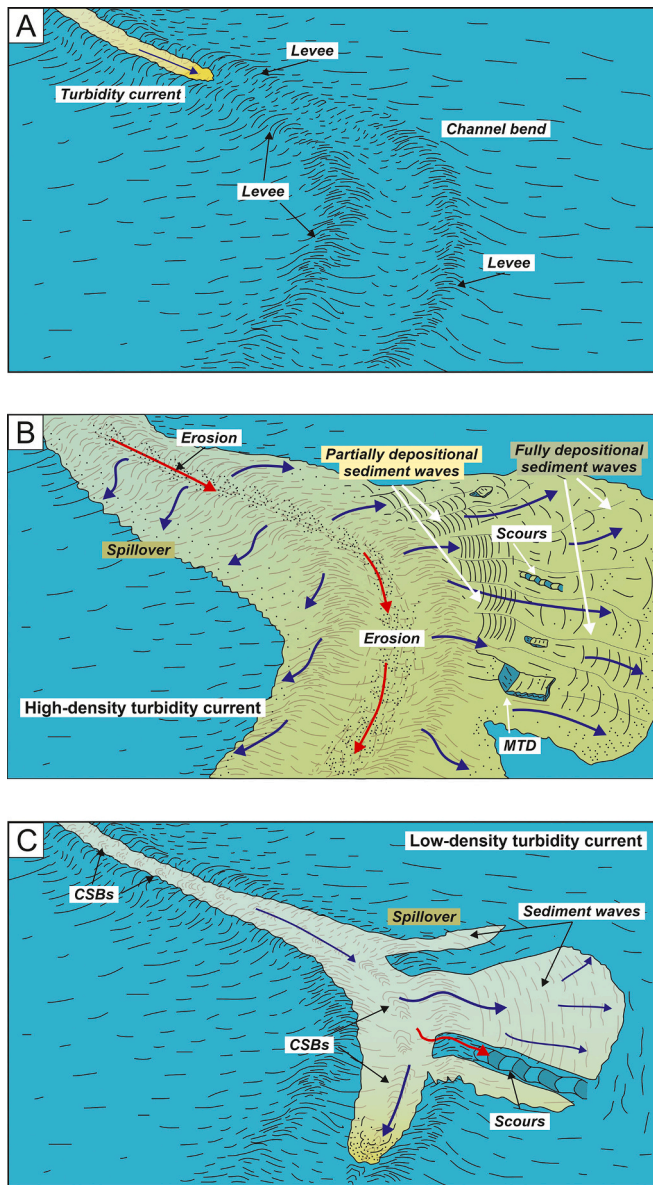
Fig. 17. Illustration of two different scenarios of downcanyon channelized turbiditic flows descending along the axial channel and approaching the sharp bend in the Carchuna Canyon (A). (B) High-density turbidity currents flowing along the Carchuna Canyon eroding the axial channel, while widespread spillover flows would form along both levees. At the channel bend, heterogeneous deposits resulting from the high-density turbidity currents vary between partially depositional sediment waves in the upper reaches of the depositional lobe to fully depositional sediment waves in the lower reaches. Erosive features and MTDs are favored by the steep slopes and the high turbulence of the turbidity currents. (C) Low-density turbidity currents flow along the Carchuna Canyon forming bedforms along the axial channel while spillover processes are localized at the channel bend, forming either depositional or erosional bedforms. Sediment wave generation would be related to recurrent overflows passing by depressed levee crests. Scour trains can be attributed to energetic and episodic flows that exceed the levee crest at the channel bend due to the orientation shift of the axial channel.

deposition rates (Migeon et al., 2000; Nakajima and Satoh, 2001; Gong et al., 2012; Morris et al., 2014). The accumulation of such sediment waves in the studied depositional lobe, plus their lateral change to subparallel lenticular bodies, would suggest the activity of recurring turbidity currents that decrease in flow velocity downslope (Fig. 18E, F). The absence of sediment waves and the occurrence of an aggradational

infilling in the lower reaches of the Carchuna depositional lobe (Fig. 18H, I) is most likely a consequence of low slope gradients and low turbulence values of turbidity currents, common in such environments (e.g., Stacey et al., 2019).

We suggest that acoustic units 4 and 2 are indicative of high-density turbidity current scenarios in the Carchuna Canyon (Fig. 17B). Under such conditions, the axial channel would be mainly characterized by erosion due to the entrainment of coarse-grained sediments by high-velocity flows, enabling the formation of widespread spillovers along both levees. At the channel bend, abundant overflows would generate an irregular seafloor forming an overbank deposit characterized by heterogeneous deposition and high sedimentation rates. These conditions would lead to a widespread occurrence of sediment waves evolving seaward, from low- to high-aggradational system, in response to the velocity decrease of overflows (Fig. 17B). The formation of scour trains cannot be discarded (Fig. 17B), considering that at likely seafloor variability in the overbank deposit could trigger hydraulic jumps. In addition, the irregular slope topography and high depositional rates would be conducive to mass movements eventually forming MTDs (Fig. 17B).

5.3.2. Low-density turbidity current scenario

Sediment drapes in submarine canyon settings can be linked to hemipelagic sediments that exhibit transparent acoustic facies (e.g., Paull et al., 2013; Tubau et al., 2015; Covault et al., 2017) or high-amplitude continuous reflections atop acoustic units that define overbank deposits (e.g., Lewis and Pantin, 2002; Zhu et al., 2010). Alternatively, drape units can be the sedimentary product of fine-grained turbidity currents (Covault et al., 2014), which tend to develop sediment waves in overbank deposits (e.g., von Lom-Keil et al., 2002; Migeon et al., 2006; Scacchia et al., 2022). In this sense, the depositional lobe of Carchuna Canyon exhibits two acoustic units (3 and 1) mainly characterized by transparent acoustic facies with undulating tops interpreted as sediment waves (Figs. 12 and 13). Considering such an arrangement, we infer that both transparent acoustic units are linked to low-density turbidity currents depositing fairly homogeneous fine-grained sediments.

In low-density turbidity current scenarios in the Carchuna Canyon setting (Fig. 17C), coarse-grained sediments would be mainly limited to the axial channel and would contribute to the generation of confined CSBs. The finer sediment fractions, in contrast, could be transferred along localized depressed stretches of the levee by top spillover currents, subsequently contributing to growth of the overbank deposit. Energetic and episodic transport pulses would exceed the levee crest in the channel bend, forming scour trains. A low-density turbidity current scenario could be active at present, considering that: (1) both CSBs and sediment waves developed in the overbank deposit are migrating today, suggesting the occurrence of repetitive turbidites along the Carchuna Canyon; (2) hemipelagic drapes have been not identified over the overbank deposits.

6. Conclusions

Detailed analysis of bedform distribution and morphology along the Carchuna Canyon, on the northern margin of the Alboran Sea, stands as a contribution to cataloguing bedform genesis in submarine canyons worldwide. Understanding the formation and maintenance of the bedforms along submarine canyons is essential because it allows us to better understand the behavior of turbidity flows and their evolution over time. Additionally, it provides valuable information on the current activity of the canyon, which might not be discernible on a broad scale. Moreover, the unique and novel combination of the methodology used in this work from the fine-scale characterization of bedforms has allowed us to contextualize the processes generated along the canyon and their implications in the lower reaches of the channel and depositional lobe. Although the flow simulation has been used in this work to describe the bedforms and to understand their formation, a multi-proxy
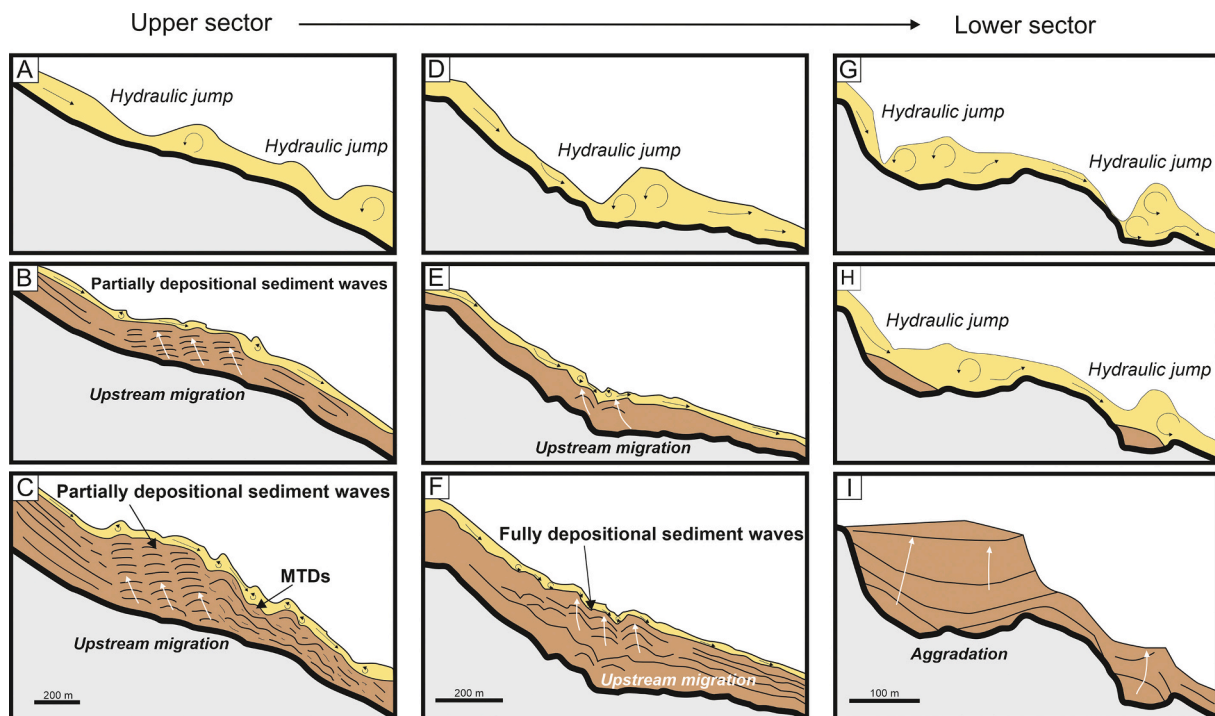
Upper sector ⟶ Lower sector

Fig. 18. Downslope deposit evolution resulting from high-density turbidity currents moving from the upper to the lower sector of the Carchuna depositional lobe over pre-existing irregular surfaces (A, D, and G). (A-C) Evolution model of the fill of the ancient seafloor in the upper sector characterized by partially depositional sediment waves truncated downstream by MTDs likely due to the steep slope gradient. (D-F) Evolution model of the fill of the ancient seafloor in the middle reaches of the depositional lobe characterized by fully depositional sediment waves; distally, sub-parallel bodies indicate the decrease in flow velocities of turbidity currents. (G-I) Evolution model of the fill of the ancient seafloor in the lower sector, where aggradational deposits evidence the low velocities of turbidity currents in this sector of the depositional lobe.

study of the bedforms is therefore essential to increase the limited knowledge of the sedimentary processes forming bedforms and understand the role of the sedimentary activity of submarine canyons in bedform generation. The main conclusions of this study are:

1. The shelf-incised Carchuna Canyon exhibits recent sedimentary activity, evidenced by net-erosional and net-depositional cyclic steps, depending on the confined/unconfined nature of the flows. The occurrence of crescentic-shaped bedforms (CSBs) (confined cyclic steps) in the axial channel of the Carchuna Canyon suggests the influence of confined sediment-laden gravity flows characterized by coarse-grained sediments descending along the channel. The variation in morphometric parameters of CSB sets along the axial channel is indicative of flow behavior variability, in turn dependent on local slope gradients that induce flow accelerations and local increases in sediment concentration.

2. Unconfined spillover flows may be generated in a sharp channel bend in the lower canyon segment, eventually triggering the formation of two types of bedforms over the depositional lobe of the Carchuna Canyon. The occurrence of depressed stretches of the levee crest favor spillovers along the channel bend and the formation of sediment waves, likely indicating recurring stripping by fine-grained turbidity currents. In contrast, more energetic and occasional downstream turbidity flows exceed the levee crest at the channel bend to focus the overflow and favor the erosion of the overbank deposit forming scour trains.

3. The overbank deposits of the Carchuna Canyon grew by means of the alternance of turbidity currents, which exhibit two contrasting patterns —likely suggesting a periodic temporal change in the behavior of the canyon as a sediment transport system. High-density turbidity currents flowing downstream favor erosion along the axial channel and a widespread spillover flow of coarse-grained sediments, giving rise to the formation of a complex arrangement of deposits and morphologies having a marked bathymetric zonation. MTDs, low-aggradational sediment waves and erosive features preferentially occur in the upper reaches, evolving downslope to fully depositional sediment waves and distal aggradation. In contrast, under the dominance of low-density turbidity currents, limited coarse-grained sediment deposition occur along the Carchuna Canyon axial channel, whereas spillover processes would be localized along the channel bend.

Supplementary data to this article can be found online at https://doi.org/10.1016/j.margeo.2024.107429.

CRediT authorship contribution statement

J. Cerrillo-Escoriza: Writing – review & editing, Writing – original draft, Visualization, Validation, Methodology, Investigation, Formal analysis, Conceptualization. **A. Micallef:** Writing – review & editing, Supervision, Software, Resources, Conceptualization. **F.J. Lobo:** Writing – review & editing, Validation, Supervision, Software, Resources, Project administration, Methodology, Investigation, Funding acquisition, Data curation, Conceptualization. **Á. Puga-Bernabéu:** Writing – review & editing, Visualization, Validation, Supervision, Resources, Project administration, Methodology, Investigation, Formal analysis, Data curation, Conceptualization. **P. Bárcenas:** Writing – review & editing, Visualization, Validation, Methodology, Formal analysis, Data curation. **I. Schulten:** Writing – review & editing, Validation, Software, Formal analysis, Data curation, Conceptualization. **R. Durán:** Writing – review & editing, Validation, Supervision, Formal analysis, Data curation. **Á. Carrión-Torrente:** Writing – review & editing, Methodology, Formal analysis, Data curation. **A. López-Quirós:** Writing – review & editing, Validation, Methodology, Formal analysis. **M. Luján:** Writing – review

Data availability

The data used in this study are posted in ZENODO repository (https://zenodo.org/) with the following DOI: https://zenodo.org/records/12754212

References

Amblas, D., Gerber, T.P., De Mol, B., Urgeles, R., Garcia-Castellanos, D., Canals, M., Pratson, L.F., Robb, N., Canning, J., 2012. Survival of a submarine canyon during long-term outbuilding of a continental margin. Geology 40, 543–546. https://doi.org/10.1130/G33178.1.

Armitage, D.A., McHargue, T., Fildani, A., Graham, S.A., 2012. Postavulsion channel evolution: Niger Delta continental slope. AAPG Bull. 96, 823–843. https://doi.org/10.1306/09131110189.

Arzola, R.G., Wynn, R.B., Lastras, G., Masson, D.G., Weaver, P.P.E., 2008. Sedimentary features and processes in the Nazaré and Setúbal submarine canyons, west Iberian margin. Mar. Geol. 250, 64–88. https://doi.org/10.1016/j.margeo.2007.12.006.

Babonneau, N., Delacourt, C., Can:couet, R., Sisavath, E., Bachèlery, P., Mazuel, A., Jorry, S.J., Deschamps, A., Ammann, J., Villeneuve, N., 2013. Direct sediment transfer from land to deep-sea: Insights into shallow multibeam bathymetry at La Réunion Island. Mar. Geol. 346, 47–57. https://doi.org/10.1016/j.margeo.2013.08.006.

Ballesteros, M., Rivera, J., Muñoz, A., Muñoz-Martín, A., Acosta, J., Carbó, A., Uchupi, E., 2008. Alboran Basin, southern Spain-Part II: Neogene tectonic implications for the orogenic float model. Mar. Petrol. Geol. 25, 75–101. https://doi.org/10.1016/j.marpetgeo.2007.05.004.

Bárcenas, P., Fernández-Salas, L.M., Macías, J., Lobo, F.J., Díaz del Río, V., 2009. Estudio morfométrico comparativo entre las ondulaciones de los prodeltas de los ríos de Andalucía Oriental. Rev. Soc. Geol. Esp. 22, 43–56.

Bárcenas, P., Lobo, F.J., Macías, J., Fernández-Salas, L.M., Díaz del Río, V., 2011. Spatial variability of surficial sediments on the northern shelf of the Alboran Sea: the effects of hydrodynamic forcing and supply of sediment by rivers. J. Iber. Geol. 37, 195–214. https://doi.org/10.5209/rev_JIGE.2011.v37.n2.8.

Bárcenas, P., Lobo, F.J., Macías, J., Fernández-Salas, L.M., López-González, N., Díaz del Río, V., 2015. Submarine deltaic geometries linked to steep, mountainous drainage basins in the northern shelf of the Alboran Sea: filling the gaps in the spectrum of deltaic deposition. Geomorphology 232, 125–144. https://doi.org/10.1016/j.geomorph.2014.11.028.

Basani, R., Janocko, M., Cartigny, M.J., Hansen, E.W., Eggenhuisen, J.T., 2014. MassFLOW-3DTM as a simulation tool for turbidity currents: Some preliminary results. In: Martinius, A.W., Ravnås, R., Howell, J.A., Steel, R.J., Wonham, J.P. (Eds.), From Depositional Systems to Sedimentary Successions on the Norwegian Continental Margin. Int. Assoc. Sedimentol. Spec. Publ, vol. 46, pp. 587–608.

Baztan, J., Berné, S., Olivet, J.L., Rabineau, M., Aslanian, D., Gaudin, M., Réhault, J.P., Canals, M., 2005. Axial incision: the key to understand submarine canyon evolution (in the western Gulf of Lion). Mar. Petrol. Geol. 22, 805–826. https://doi.org/10.1016/j.marpetgeo.2005.03.011.

Bosman, A., Romagnoli, C., Madricardo, F., Correggiari, A., Remia, A., Zubalich, R., Fogarin, S., Kruss, A., Trincardi, F., 2020. Short-term evolution of Po della Pila delta lobe from time lapse high-resolution multibeam bathymetry (2013–2016). Estuar. Coast. Shelf Sci. 233, 106533. https://doi.org/10.1016/j.ecss.2019.106533.

Brun, L., Pairaud, I., Jacinto, R.S., Garreau, P., Dennielou, B., 2023. Strong hydrodynamic processes observed in the Mediterranean Cassidaigne submarine canyon. Front. Mar. Sci. 10, 1–17. https://doi.org/10.3389/fmars.2023.1078831.

Bührig, L.H., Colombera, L., Patacci, M., Mountney, N.P., McCaffrey, W.D., 2022. A global analysis of controls on submarine-canyon geomorphology. Earth Sci. Rev. 233, 104150. https://doi.org/10.1016/j.earscirev.2022.104150.

Cabrera, C., Puig, P., Durán, R., Fabri, M.C., Guerin, C., Lo Iacono, C., Huvenne, V.A.I., 2024. Geomorphology and evolution of the Blanes Canyon (NW Mediterranean). New insights from high resolution mapping of vertical cliffs. Geomorphology 461, 109290. https://doi.org/10.1016/j.geomorph.2024.109290.

Carter, L., Carter, R.M., Nelson, C.S., Fulthorpe, C.S., Neil, H.L., 1990. Evolution of Pliocene to recent abyssal sediment waves on Bounty Channel levees, New Zealand. Mar. Geol. 95, 97–109. https://doi.org/10.1016/0025-3227(90)90045-X.

Cartigny, M.J.B., Postma, G., van den Berg, J.H., Mastbergen, D.R., 2011. A comparative study of sediment waves and cyclic steps based on geometries, internal structures and numerical modeling. Mar. Geol. 280, 40–56. https://doi.org/10.1016/j.margeo.2010.11.006.

Cartigny, M.J.B., Eggenhuisen, J.T., Hansen, E.W.M., Postma, G., 2013. Concentration-dependent flow stratification in experimental high-density turbidity currents and their relevance to turbidite facies models. J. Sediment. Res. 83, 1046–1064. https://doi.org/10.2110/jsr.2013.71.

Cartigny, M.J.B., Ventra, D., Postma, G., van Den Berg, J.H., 2014. Morphodynamics and sedimentary structures of bedforms under supercritical-flow conditions: New insights from flume experiments. Sedimentology 61, 712–748. https://doi.org/10.1111/sed.12076.

Casalbore, D., Romagnoli, C., Bosman, A., Chiocci, F.L., 2014. Large-scale seafloor waveforms on the flanks of insular volcanoes (Aeolian Archipelago, Italy), with inferences about their origin. Mar. Geol. 355, 318–329. https://doi.org/10.1016/j.margeo.2014.06.007.

Casalbore, D., Falcini, F., Martorelli, E., Morelli, E., Bosman, A., Calarco, M., Chiocci, F.L., 2018. Characterization of overbanking features on the lower reach of the Gioia-Mesima canyon-channel system (southern Tyrrhenian Sea) through integration of morpho-stratigraphic data and physical modelling. Prog. Oceanogr. 169, 66–78. https://doi.org/10.1016/j.pocean.2018.02.020.

Cerrillo-Escoriza, J., Lobo, F.J., Puga-Bernabéu, Á., Rueda, J.L., Bárcenas, P., Sánchez-Guillamón, O., Serna Quintero, J.M., Pérez Gil, J.L., Murillo, Y., Caballero-Herrera, J.A., López-Quirós, A., Mendes, I., Pérez-Asensio, J.N., 2023. Origin and driving mechanisms of marine litter in the shelf-incised Motril, Carchuna, and Calahonda canyons (northern Alboran Sea). Front. Mar. Sci. 10, 1098927. https://doi.org/10.3389/fmars.2023.1098927.

Cerrillo-Escoriza, J., Lobo, F.J., Puga-Bernabéu Bárcenas, P., Mendes, I., Pérez-Asensio, J.N., Durán, R., Andersen, T.J., Carrión-Torrente, García, M., López-Quirós, A., Luján, M., Mena, A., Sánchez-Guillamón, O., Sánchez, M.J., 2024. Variable downcanyon morphology controlling the recent activity of shelf-incised submarine canyons (Alboran Sea, western Mediterranean). Geomorphology 453, 109127. https://doi.org/10.1016/j.geomorph.2024.109127.

Chen, Y., Parsons, D.R., Simmons, S.M., Williams, R., Cartigny, M.J.B., Hughes Clarke, J.E., Stacey, C.D., Hage, S., Talling, P.J., Azpiroz-Zabala, M., Clare, M.A., Hizzett, J.L., Heijnen, M.S., Hunt, J.E., Lintern, D.G., Sumner, E.J., Vellinga, A.J., Vendettuoli, D., 2021. Knickpoints and crescentic bedform interactions in submarine channels. Sedimentology 68, 1358–1377. https://doi.org/10.1111/sed.12886.

Comas, M.C., García-Dueñas, V., Jurado, M.J., 1992. Neogene tectonic evolution of the Alboran Sea from MCS data. In: Maldonado, A. (Ed.), The Alboran Sea. Geo-Mar. Lett, vol. 12, pp. 157–164. https://doi.org/10.1007/BF02084927.

Covault, J.A., Fildani, A., Romans, B.W., McHargue, T., 2011. The natural range of submarine canyon-and-channel longitudinal profiles. Geosphere 7, 313–332. https://doi.org/10.1130/GES00610.1.

Covault, J.A., Kostic, S., Paull, C.K., Ryan, H., Fildani, A., 2014. Submarine channel initiation, filling, and maintenance from sea-floor geomorphology and morphodynamic modelling of cyclic steps. Sedimentology 61, 1031–1054. https://doi.org/10.1111/sed.12084.

Covault, J.A., Kostic, S., Paull, C.K., Sylvester, Z., Fildani, A., 2016. Cyclic steps and related supercritical bedforms: building blocks of deep-water depositional systems, western North America. Mar. Geol. 393, 4–20. https://doi.org/10.1016/j.margeo.2016.12.009.

Covault, J.A., Kostic, S., Paull, C.K., Sylvester, Z., Fildani, A., 2017. Cyclic steps and related supercritical bedforms: Building blocks of deep-water depositional systems,

western North America. Mar. Geol. 393, 4–20. https://doi.org/10.1016/J.MARGEO.2016.12.009.

DeGeest, A.L., Mullenbach, B.L., Puig, P., Nittrouer, C.A., Drexler, T.M., Durrieu de Madron, X., Orange, D.L., 2008. Sediment accumulation in the western Gulf of Lions, France: the role of Cap de Creus Canyon in linking shelf and slope sediment dispersal systems. Cont. Shelf Res. 28, 2031–2047. https://doi.org/10.1016/j.csr.2008.02.008.

Dietrich, P., Ghienne, J.F., Normandeau, A., Lajeunesse, P., 2016. Upslope-migrating bedforms in a proglacial Sandur delta: Cyclic steps from river-derived underflows? J. Sediment. Res. 86, 113–123. https://doi.org/10.2110/jsr.2016.4.

Dobbs, S.C., Paull, C.K., Lundsten, E.M., Gwiazda, R., Caress, D.W., McGann, M., Coholich, M.M., Walton, M.A.L., Nieminski, N.M., McHargue, T., Graham, S.A., 2023. Sediment gravity flow frequency offshore Central California diminished significantly following the last Glacial Maximum. Front. Mar. Sci. 10, 1–12. https://doi.org/10.3389/fmars.2023.1099472.

Droghei, R., Falcini, F., Casalbore, D., Martorelli, E., Mosetti, R., Sannino, G., Santoleri, R., Chiocci, F.L., 2016. The role of Internal Solitary Waves on deep-water sedimentary processes: the case of up-slope migrating sediment waves off the Messina Strait. Sci. Rep. 6, 1–8. https://doi.org/10.1038/srep36376.

Droz, L., Marsset, T., Ondréas, H., Lopez, M., Savoye, B., Spy-Anderson, F.-L., 2003. Architecture of an active mud-rich turbidite system: the Zaire Fan (Congo–Angola margin Southeast Atlantic) results from ZaïAngo 1 and 2 cruises. AAPG Bull. 87, 1145–1168. https://doi.org/10.1306/03070300013.

Ercilla, G., Alonso, B., Baraza, J., 1994. Post-Calabrian sequence stratigraphy of the northwestern Alboran Sea (southwestern Mediterranean). Mar. Geol. 120, 249–265. https://doi.org/10.1016/0025-3227(94)90061-2.

Ercilla, G., Juan, C., Hernández-Molina, F.J., Bruno, M., Estrada, F., Alonso, B., Casas, D., Farran, M., Llave, E., García, M., Vázquez, J.T., D'Acremont, E., Gorini, C., Palomino, D., Valencia, J., El Moumni, B., Ammar, A., 2016. Significance of bottom currents in deep-sea morphodynamics: an example from the Alboran Sea. Mar. Geol. 378, 157–170. https://doi.org/10.1016/j.margeo.2015.09.007.

Fabres, J., Calafat, A., Sanchez-Vidal, A., Canals, M., Heussner, S., 2002. Composition and spatio-temporal variability of particle fluxes in the Western Alboran Gyre, Mediterranean Sea. J. Mar. Syst. 33–34, 431–456. https://doi.org/10.1016/S0924-7963(02)00070-2.

Fabri, M.C., Bargain, A., Pairaud, I., Pedel, L., Taupier-Letage, I., 2017. Cold-water coral ecosystems in Cassidaigne Canyon: an assessment of their environmental living conditions. Deep. Res. Part II Top. Stud. Oceanogr. 137, 436–453. https://doi.org/10.1016/j.dsr2.2016.06.006.

Fernández-Salas, L.M., Dabrio, C.J., Goy, J.L., Díaz del Río, V., Zazo, C., Lobo, F.J., Sanz, J.L., Lario, J., 2009. Land-sea correlation between late Holocene coastal and infralittoral deposits in the SE Iberian Peninsula (Western Mediterranean). Geomorphology 104, 4–11. https://doi.org/10.1016/j.geomorph.2008.05.013.

Fernane, I., Matougui, R., Amarni, N., Belkessa, R., 2022. Variation in canyon morphology and their relationship with tectonic: the example of the western Algerian margin. Arab. J. Geosci. 15, 254. https://doi.org/10.1007/s12517-022-09566-6.

Fildani, A., Normark, W.R., Kostic, S., Parker, G., 2006. Channel formation by flow stripping: Large-scale scour features along the Monterey East Channel and their relation to sediment waves. Sedimentology 53, 1265–1287. https://doi.org/10.1111/j.1365-3091.2006.00812.x.

Fildani, A., Hubbard, S.M., Covault, J.A., Maier, K.L., Romans, B.W., Traer, M., Rowland, J.C., 2013. Erosion at inception of deep-sea channels. Mar. Petrol. Geol. 41, 48–61. https://doi.org/10.1016/j.marpetgeo.2012.03.006.

Flood, R.D., Giosan, L., 2002. Migration history of a fine-grained abyssal sediment wave on the Bahama Outer Ridge. Mar. Geol. 192, 259–273. https://doi.org/10.1016/S0025-3227(02)00558-3.

FLOW-3D® Version 2022R1 [FLOW-3D HYDRO], 2022. Santa Fe. Flow Science, Inc., NM. https://www.flow3d.com.

Folk, R.L., 1954. The distinction between grain size and mineral composition in sedimentary rock nomenclature. J. Geol. 62, 344–359. https://doi.org/10.1086/626171.

Gamberi, F., Rovere, M., Dykstra, M., Kane, I.A., Kneller, B.C., 2013. Integrating modern seafloor and outcrop data in the analysis of slope channel architecture and fill. Mar. Petrol. Geol. 41, 83–103. https://doi.org/10.1016/j.marpetgeo.2012.04.002.

García, M., Alonso, B., Ercilla, G., Gràcia, E., 2006. The tributary valley systems of the Almeria Canyon (Alboran Sea, SW Mediterranean): sedimentary architecture. Mar. Geol. 226, 207–223. https://doi.org/10.1016/j.margeo.2005.10.002.

Ge, Z., Nemec, W., Gawthorpe, R.L., Hansen, E.W.M., 2017. Response of unconfined turbidity current to normal-fault topography. Sedimentology 64, 932–959. https://doi.org/10.1111/sed.12333.

Gerber, T.P., Amblas, D., Wolinsky, M.A., Pratson, L.F., Canals, M., 2009. A model for the long-profile shape of submarine canyons. Case Rep. Med. 114, 1–24. https://doi.org/10.1029/2008JF001190.

Goldfinger, C., Morey, A.E., Nelson, C.H., Gutiérrez-Pastor, J., Johnson, J.E., Karabanov, E., Chaytor, J., Eriksson, A., Winkler, M., Kalk, P., Camarero, A., Morri, C., Dunhill, G., Ramos, L., Raab, A., Pisias, N., Pourmanoutscheri, M., Van Rooij, D., Amy, L., Liu, C.C.C., Moser, C., Etheridge, D., Stenner, H., Popham, C., McKee, C., McMillan, D., Crosby, C., Schmid, S., Gracia, E., Lovelady, S., Romsos, C., Rinterknecht, V., Robison, R., Casas, D., Charlet, F., Hinrichsen, B., Oxford, J., Marin, M., Mas, M., Montes, S., Villalonga, R., Vizcaino, A., Jimenez, S., Pedrosa, M., Perez, S., Perez, A., Turra, A., Lamas, D., Falcon, H., Baranco, A., Schwartz, D., Zoback, M. Lou, Fumal, T., Niemi, T., 2007. Rupture lengths and temporal history of significant earthquakes on the offshore and north coast segments of the Northern San Andreas Fault based on turbidite stratigraphy. Earth Planet. Sci. Lett. 254, 9–27. https://doi.org/10.1016/j.epsl.2006.11.017.

Gong, C., Wang, Y., Peng, X., Li, W., Qiu, Y., Xu, S., 2012. Sediment waves on the South China Sea Slope off southwestern Taiwan: Implications for the intrusion of the Northern Pacific Deep Water into the South China Sea. Mar. Petrol. Geol. 32, 95–109. https://doi.org/10.1016/j.marpetgeo.2011.12.00.

Hage, S., Cartigny, M.J.B., Clare, M.A., Sumner, E.J., Vendettuoli, D., Clarke, J.E.H., Hubbard, S.M., Talling, P.J., Gwyn Lintern, D., Stacey, C.D., Englert, R.G., Vardy, M. E., Hunt, J.E., Yokokawa, M., Parsons, D.R., Hizzett, J.L., Azpiroz-Zabala, M., Vellinga, A.J., 2018. How to recognize crescentic bedforms formed by supercritical turbidity currents in the geologic record: Insights from active submarine channels. Geology 46, 563–566. https://doi.org/10.1130/G40095.1.

Hagen, R.A., Bergersen, D.D., Moberly, R., Colbourn, W.T., 1994. Morphology of a large meandering submarine canyon system on the Peru-Chile forearc. Mar. Geol. 119, 7–38. https://doi.org/10.1016/0025-3227(94)90138-4.

Hansen, L.A.S., Callow, R.H.T., Kane, I.A., Gamberi, F., Rovere, M., Cronin, B.T., Kneller, B.C., 2015. Genesis and character of thin-bedded turbidites associated with submarine channels. Mar. Petrol. Geol. 67, 852–879. https://doi.org/10.1016/j.marpetgeo.2015.06.007.

Heimsund, S., Hansen, E.W., Nemec, W., 2002. Computational 3-D fluid-dynamics model for sediment transport, erosion and deposition by turbidity currents. In: Abstracts, IAS 16th International Sedimentological Congress, pp. 151–152. https://doi.org/10.13140/RG.2.2.26785.76645.

Heiniö, P., Davies, R.J., 2009. Trails of depressions and sediment waves along submarine channels on the continental margin of Espirito Santo Basin, Brazil. Bull. Geol. Soc. Am. 121, 698–711. https://doi.org/10.1130/B26190.1.

Hesse, R., 1995. Long-distance correlation of spillover turbidites on the western levee of the Northwest Atlantic Mid-Ocean Channel (NAMOC), Labrador Sea. In: Pickering, K.T., Hiscott, R.N., Kenyon, N.H., Ricci Lucchi, F., Smith, R.D.A. (Eds.), Atlas of Deep Water Environments: Architectural Style in Turbidite Systems. Chapman and Hall, London, pp. 276–281. https://doi.org/10.1007/978-94-011-1234-5_41.

Hiscott, R.N., Hall, F.R., Pirmez, C., Flood, R., Piper, D., Klaus, A., Peterson, L., 1997. Turbidity-current overspill from the Amazon channel: texture of the silt/sand load, paleoflow from anisotropy of magnetic susceptibility and implications for flow processes. In: Proceedings of the Ocean Drilling Program, Scientific Results, 155, p. 53e78. https://doi.org/10.2973/odp.proc.sr.155.202.1997.

Hiscott, R.N., Aksu, A.E., Flood, R.D., Kostylev, V., Yaşar, D., 2013. Widespread overspill from a saline density-current channel and its interaction with topography on the south-West Black Sea shelf. Sedimentology 60, 1639–1667. https://doi.org/10.1111/sed.12071.

Hizzett, J.L., Hughes Clarke, J.E., Sumner, E.J., Cartigny, M.J.B., Talling, P.J., Clare, M.A., 2017. Which triggers produce the most erosive, frequent and longest runout turbidity currents on deltas? Geophys. Res. Lett. 45, 855–863. https://doi.org/10.1002/2017GL075751.

Hughes Clarke, J.E., Marques, C.R.V., Pratomo, D., 2014. Imaging active mass-wasting and sediment flows on a fjord delta, Squamish, British Columbia. In: Krastel, S. (Ed.), Submarine Mass Movements and Their Consequences: Advances in Natural and Technological Hazards Research, 37, pp. 249–260. https://doi.org/10.1007/978-3-319-00972-8_22.

Izumi, N., 2004. The formation of submarine gullies by turbidity currents. J. Geophys. Res. Ocean. 109, 1–13. https://doi.org/10.1029/2003jc001898.

Jipa, D.C., Panin, N., 2020. Narrow shelf canyons vs. wide shelf canyons: two distinct types of Black Sea submarine canyons. Quat. Int. 540, 120–136. https://doi.org/10.1016/j.quaint.2018.08.006.

Kertznus, V., Kneller, B., 2009. Clinoform quantification for assessing the effects of external forcing on continental margin development. Basin Res. 21, 738–758. https://doi.org/10.1111/j.1365-2117.2009.00411.x.

Khripounoff, A., Crassous, P., Lo Bue, N., Dennielou, B., Silva Jacinto, R., 2012. Different types of sediment gravity flows detected in the Var submarine canyon (northwestern Mediterranean Sea). Prog. Oceanogr. 106, 138–153. https://doi.org/10.1016/j.pocean.2012.09.001.

Kneller, B., Buckee, C., 2000. The structure and fluid mechanics of turbidity currents: a review of some recent studies and their geological implications. Sedimentology 47, 62–94. https://doi.org/10.1046/j.1365-3091.2000.047s1062.x.

Kneller, B., McCaffrey, W.D., 1995. Modelling the effects of salt-induced topography on deposition from turbidity currents. In: GCSSEPM Foundation 16th Annual Research Conference Salt, Sediment and Hydrocarbons, 16. SEPM, pp. 137–145. https://doi.org/10.5724/gcs.95.16.0137.

Kostic, S., 2011. Modeling of submarine cyclic steps: Controls on their formation, migration, and architecture. Geosphere 7, 294–304. https://doi.org/10.1130/GES00601.1.

Kostic, S., 2014. Upper flow regime bedforms on levees and continental slopes: turbidity current flow dynamics in response to fine-grained sediment waves. Geosphere 10, 1094–1103. https://doi.org/10.1130/GES01015.1.

Kostic, S., Parker, G., 2006. The response of turbidity currents to a canyon-fan transition: Internal hydraulic jumps and depositional signatures. J. Hydraul. Res. 44, 631–653. https://doi.org/10.1080/00221686.2006.9521713.

Kostic, S., Sequeiros, O., Spinewine, B., Parker, G., 2010. Cyclic steps: a phenomenon of supercritical shallow flow from the high mountains to the bottom of the ocean. J. Hydro Environ. Res. 3, 167–172. https://doi.org/10.1016/j.jher.2009.10.002.

Kubo, Y., Nakajima, T., 2002. Laboratory experiments and numerical simulation of sediment-wave formation by turbidity currents. Mar. Geol. 192, 105–121. https://doi.org/10.1016/S0025-3227(02)00551-0.

Lamb, M.P., Parsons, J.D., Mullenbach, B.L., Finlayson, D.P., Orange, D.L., Nittrouer, C.A., 2008. Evidence for superelevation, channel incision, and formation of cyclic steps by turbidity currents in Eel Canyon, California. Bull. Geol. Soc. Am. 120, 463–475. https://doi.org/10.1130/B26184.1.

Lario, J., Zazo, C., Goy, J.L., 1999. Fases de progradación y evolución morfosedimentaria de la flecha litoral de Calahonda (Granada) durante el Holoceno. Estud. Geol. 55, 247–250. https://doi.org/10.3989/egeol.99555-6164.

Lastras, G., Canals, M., Urgeles, R., Amblas, D., Ivanov, M., Droz, L., Dennielou, B., Fabrés, J., Schoolmeester, T., Akhmetzhanov, A., Orange, D., García-García, A., 2007. A walk down the Cap de Creus canyon, Northwestern Mediterranean Sea: recent processes inferred from morphology and sediment bedforms. Mar. Geol. 246, 176–192. https://doi.org/10.1016/j.margeo.2007.09.002.

Leeder, M.R., 1999. Sedimentology and Sedimentary Basins: from Turbulence to Tectonics. Blackwell Science, Oxford. https://doi.org/10.1017/S0016756800224618.

Lewis, K.B., Pantin, H.M., 2002. Channel-axis, overbank and drift sediment waves in the southern Hikurangi Trough, New Zealand. Mar. Geol. 192, 123–151. https://doi.org/10.1016/S0025-3227(02)00552-2.

Li, L., Gong, C., 2018. Gradual transition from net erosional to net depositional cyclic steps along the submarine distributary channel thalweg in the Rio muni Basin: a joint 3-D seismic and numerical approach. Case Rep. Med. 123, 2087–2106. https://doi.org/10.1029/2017JF004513.

Li, C., Ma, M., Lv, C., Zhang, G., Chen, G., Yan, Y., Bi, G., 2017. Sedimentary differences between different segments of the continental slope-parallel Central Canyon in the Qiongdongnan Basin on the northern margin of the South China Sea. Mar. Petrol. Geol. 88, 127–140. https://doi.org/10.1016/j.marpetgeo.2017.08.009.

Liquete, C., Arnau, P., Canals, M., Colas, S., 2005. Mediterranean river systems of Andalusia, southern Spain, and associated deltas: a source to sink approach. Mar. Geol. 222–223, 471–495. https://doi.org/10.1016/j.margeo.2005.06.033.

Lo Iacono, C., Guillén, J., Guerrero, Q., Durán, R., Wardell, C., Hall, R.A., Aslam, T., Carter, G.D., Gales, J.A., Huvenne, V.A.I., 2020. Bidirectional bedform fields at the head of a submarine canyon (NE Atlantic). Earth Planet. Sc. Lett. 542, 116321. https://doi.org/10.1016/j.epsl.2020.116321.

Lobo, F.J., Goff, J.A., Mendes, I., Bárcenas, P., Fernández-Salas, L.M., Martín-Rosales, W., Macías, J., Díaz del Río, V., 2015. Spatial variability of prodeltaic undulations on the Guadalfeo River prodelta: support to the genetic interpretation as hyperpycnal flow deposits. Mar. Geophys. Res. 36, 309–333. https://doi.org/10.1007/s11001-014-9233-9.

Lowe, D.R., 1982. Sediment gravity flows; II. Depositional models with special reference to the deposits of high- density turbidity currents. J. Sediment. Res. 52, 279–297. https://doi.org/10.1306/212F7F31-2B24-11D7-8648000102C1865D.

Macdonald, H.A., Wynn, R.B., Huvenne, V.A., Peakall, J., Masson, D.G., Weaver, P.P., McPhail, S.D., 2011. New insights into the morphology, fill, and remarkable longevity (N0.2 my) of modern deep-water erosional scours along the Northeast Atlantic margin. Geosphere 7, 845–867. https://doi.org/10.1130/GES00611.1.

Maier, K.L., Fildani, A., Paull, C.K., Graham, S.A., McHargue, T.R., Caress, D.W., McGann, M., 2011. The elusive character of discontinuous deep-water channels: new insights from Lucia Chica channel system, offshore California. Geology 39, 327–330. https://doi.org/10.1130/G31589.1.

Maier, K.L., Fildani, A., Paull, C.K., McHargue, T.R., Graham, S.A., Caress, D.W., 2013. Deep-sea channel evolution and stratigraphic architecture from inception to abandonment from high-resolution Autonomous Underwater Vehicle surveys offshore Central California. Sedimentology 60, 935–960. https://doi.org/10.1111/j.1365-3091.2012.01371.x.

Maier, K.L., Rosenberger, K.J., Paull, C.K., Gwiazda, R., Gales, J., Lorenson, T., Barry, J.P., Talling, P.J., McGann, M., Xu, J., Lundsten, E., Anderson, K., Litvin, S.Y., Parsons, D.R., Clare, M.A., Simmons, S.M., Sumner, E.J., Cartigny, M.J.B., 2019. Sediment and organic carbon transport and deposition driven by internal tides along Monterey Canyon, offshore California. In: Deep. Res. Part I Oceanogr. Res. Pap, 153, p. 103108. https://doi.org/10.1016/j.dsr.2019.103108.

Maier, K.L., Paull, C.K., Caress, D.W., Anderson, K., Nieminski, N.M., Lundsten, E., Erwin, B.E., Gwiazda, R., Fildani, A., 2020. Submarine-fan development revealed by integrated high-resolution datasets from La Jolla fan, offshore California, U.S.a. J. Sediment. Res. 90, 468–479. https://doi.org/10.2110/jsr.2020.22.

Marsset, T., Ballas, G., Munteanu, I., Aiken, C., Ion, G., Pitel-Roudaut, M., Dupont, P., 2022. Tectonic-sedimentary architecture of surficial deposits along the continental slope offshore Romania (North of the Viteaz Canyon, Western Black Sea): Impact on sediment instabilities. Glob. Planet. Chang. 208, 103708. https://doi.org/10.1016/j.gloplacha.2021.103708.

Martinez-Lamas, R., Toucanne, S., Debret, M., Riboulot, V., Deloffre, J., Boissier, A., Cheron, S., Pitel, M., Bayon, G., Giosan, L., Soulet, G., 2020. Linking Danube River activity to Alpine Ice-Sheet fluctuations during the last glacial (ca. 33–17 ka BP): Insights into the continental signature of Heinrich Stadials. Quat. Sci. Rev. 229, 106136. https://doi.org/10.1016/j.quascirev.2019.106136.

Mas, V., Mulder, T., Dennielou, B., Schmidt, S., Khripounoff, A., Savoye, B., 2010. Multiscale spatio-temporal variability of sedimentary deposits in the Var turbidite system (North-Western Mediterranean Sea). Mar. Geol. 275, 37–52. https://doi.org/10.1016/j.margeo.2010.04.006.

Maselli, V., Kneller, B., Taiwo, O.L., Iacopini, D., 2019. Sea floor bedforms and their influence on slope accommodation. Mar. Petrol. Geol. 102, 625–637. https://doi.org/10.1016/j.marpetgeo.2019.01.021.

Maselli, V., Micallef, A., Normandeau, A., Oppo, D., Iacopini, D., Green, A., Ge, Z., 2021. Active faulting controls bedform development on a deep-water fan. Geology 49, 1495–1500. https://doi.org/10.1130/G49206.1.

Masqué, P., Fabres, J., Canals, M., Sanchez-Cabeza, J.A., Sanchez-Vidal, A., Cacho, I., Calafat, A.M., Bruach, J.M., 2003. Accumulation rates of major constituents of hemipelagic sediments in the deep Alboran Sea: a centennial perspective of sedimentary dynamics. Mar. Geol. 193, 207–233. https://doi.org/10.1016/S0025-3227(02)00593-5.

Mazières, A., Gillet, H., Castelle, B., Mulder, T., Guyot, C., Garlan, T., Mallet, C., 2014. High-resolution morphobathymetric analysis and evolution of Capbreton submarine canyon head (Southeast Bay of Biscay—French Atlantic Coast) over the last decade using descriptive and numerical modeling. Mar. Geol. 351, 1–12. https://doi.org/10.1016/j.margeo.2014.03.001.

Micallef, A., Mountjoy, J.J., Canals, M., Lastras, G., 2012. Deep-seated bedrock landslides and submarine canyon evolution in an active tectonic margin: Cook Strait, New Zealand. In: Yamada, Y., Kawamura, K., Ikehara, K., Ogawa, Y., Urgeles, R., Mosher, D., Chaytor, J.D., Strasser, M.C. (Eds.), Submarine Mass Movements and their Consequences. Springer, London, pp. 201–212. https://doi.org/10.1007/978-94-007-2162-3_18.

Micallef, A., Ribó, M., Canals, M., Puig, P., Lastras, G., Tubau, X., 2014. Space-for-time substitution and the evolution of a submarine canyon-channel system in a passive progradational margin. Geomorphology 221, 34–50. https://doi.org/10.1016/j.geomorph.2014.06.008.

Migeon, S., Savoye, B., Faugeres, J.C., 2000. Quaternary development of migrating sediment waves in the Var deep-sea fan: distribution, growth pattern, and implication for levee evolution. Sediment. Geol. 133, 265–293. https://doi.org/10.1016/S0037-0738(00)00043-9.

Migeon, S., Savoye, B., Zanella, E., Mulder, T., Faugères, J.C., Weber, O., 2001. Detailed seismic-reflection and sedimentary study of turbidite sediment waves on the var sedimentary ridge (SE France): significance for sediment transport and deposition and for the mechanisms of sediment-wave construction. Mar. Petrol. Geol. 18, 179–208. https://doi.org/10.1016/S0264-8172(00)00060-X.

Migeon, S., Savoye, B., Babonneau, N., Andersson, F.L.S., 2004. Processes of sediment-wave construction along the present Zaire deep-sea meandering channel: Role of meanders and flow stripping. J. Sediment. Res. 74, 580–598. https://doi.org/10.1306/091603740580.

Migeon, S., Mulder, T., Savoye, B., Sage, F., 2006. The Var turbidite system (Ligurian Sea, northwestern Mediterranean) - Morphology, sediment supply, construction of turbidite levee and sediment waves: Implications for hydrocarbon reservoirs. Geo-Mar. Lett. 26, 361–371. https://doi.org/10.1007/s00367-006-0047-x.

Mitchell, N.C., 2005. Interpreting long-profiles of canyons in the USA Atlantic continental slope. Mar. Geol. 214, 75–99. https://doi.org/10.1016/j.margeo.2004.09.005.

Mitchell, N.C., 2006. Morphologies of knickpoints in submarine canyons. Geol. Soc. Am. Bull. 118, 589–605. https://doi.org/10.1130/B25772.1.

Morris, E.A., Hodgson, D.M., Brunt, R.L., Flint, S.S., 2014. Origin, evolution and anatomy of silt-prone submarine external levées. Sedimentology 61, 1734–1763. https://doi.org/10.1111/sed.12114.

Mountjoy, J.J., Barnes, P.M., Pettinga, J.R., 2009. Morphostructure and evolution of submarine canyons across an active margin: Cook Strait sector of the Hikurangi margin, New Zealand. Mar. Geol. 260, 45–68. https://doi.org/10.1016/j.margeo.2009.01.006.

Mulder, T., Alexander, J., 2001. The physical character of subaqueous sedimentary density flow and their deposits. Sedimentology 48, 269–299. https://doi.org/10.1046/j.1365-3091.2001.00360.x.

Muñoz, A., Elvira, E., León, C., Acosta, J., 2017. Atlas of Bedforms in the Western Mediterranean. In: Guillén, J., Acosta, J., Latino Chiocci, F., Palanques, A. (Eds.), Atlas of Bedforms in the Western Mediterranean, vol. 38. Springer, pp. 247–252. https://doi.org/10.1007/978-3-319-33940-5.

Nakajima, T., Satoh, M., 2001. The formation of large mudwaves by turbidity currents on the levees of the Toyama deep-sea channel, Japan Sea. Sedimentology 48, 435–463. https://doi.org/10.1046/j.1365-3091.2001.00373.x.

Normandeau, A., Lajeunesse, P., Poiré, A.G., Francus, P., 2016. Morphological expression of bedforms formed by supercritical sediment density flows on four fjord-lake deltas of the South-Eastern Canadian Shield (Eastern Canada). Sedimentology 63, 2106–2129. https://doi.org/10.1111/sed.12298.

Normandeau, A., Campbell, D.C., Cartigny, M.J.B., 2019. The influence of turbidity currents and contour currents on the distribution of deep-water sediment waves offshore eastern Canada. Sedimentology 66, 1746–1767. https://doi.org/10.1111/sed.12557.

Normandeau, A., Lajeunesse, P., Ghienne, J.F., Dietrich, P., 2022. Detailed Seafloor Imagery of Turbidity Current Bedforms Reveals New Insight into Fine-Scale Near-Bed Processes. Geophys. Res. Lett. 49. https://doi.org/10.1029/2021GL097389.

Normark, W.R., Hess, G.R., Stow, D.A.V., Bowen, A.J., 1980. Sediment waves on the Monterey fan levee: a preliminary physical interpretation. Mar. Geol. 37, 1–18. https://doi.org/10.1016/0025-3227(80)90009-2.

Normark, W.R., Piper, D.J., Posamentier, H., Pirmez, C., Migeon, S., 2002. Variability in form and growth of sediment waves on turbidite channel levees. Mar. Geol. 192, 23–58. https://doi.org/10.1016/S0025-3227(02)00548-0.

Nyberg, B., Helland-Hansen, W., Gawthorpe, R.L., Sandbakken, P., Eide, C.H., Sømme, T., Hadler-Jacobsen, F., Leiknes, S., 2018. Revisiting morphological relationships of modern source-to-sink segments as a first-order approach to scale ancient sedimentary systems. Sediment. Geol. 373, 111–133. https://doi.org/10.1016/j.sedgeo.2018.06.007.

Ono, K., Naruse, H., Yao, Q., Cai, Z., Fukuda, S., Yokokawa, M., 2023. Multiple Scours and Upward Fining Caused by Hydraulic Jumps: Implications for the Recognition of Cyclic steps in the Deepwater Stratigraphic Record. J. Sediment. Res. 93, 243–255. https://doi.org/10.2110/jsr.2021.14.

Ortega-Sánchez, M., Lobo, F.J., López-Ruiz, A., Losada, M.A., Fernández-Salas, L.M., 2014. The influence of shelf-indenting canyons and infralittoral prograding wedges on coastal morphology: the Carchuna system in Southern Spain. Mar. Geol. 347, 107–122. https://doi.org/10.1016/j.margeo.2013.11.006.

Palanques, A., El Khatab, M., Puig, P., Masqué, P., Sánchez-Cabeza, J.A., Isla, E., 2005. Downward particle fluxes in the Guadiaro submarine canyon depositional system

(north-western Alboran Sea), a river flood dominated system. Mar. Geol. 220, 23–40. https://doi.org/10.1016/j.margeo.2005.07.004.

Palanques, A., Guillén, J., Puig, P., Durrieu de Madron, X., 2008. Storm-driven shelf-to-canyon suspended sediment transport at the southwestern Gulf of Lions. Cont. Shelf Res. 28, 1947–1956. https://doi.org/10.1016/j.csr.2008.03.020.

Palanques, A., Puig, P., Durrieu de Madron, X., Sanchez-Vidal, A., Pasqual, C., Martín, J., Calafat, A., Heussner, S., Canals, M., 2012. Sediment transport to the deep canyons and open-slope of the western Gulf of Lions during the 2006 intense cascading and open-sea convection period. Prog. Oceanogr. 106, 1–15. https://doi.org/10.1016/j.pocean.2012.05.002.

Paull, C.K., Ussler III, W., Caress, D.W., Lundsten, E., Covault, J.A., Maier, K.L., Xu, J., Augenstein, S., 2010. Origins of large crescent-shaped bedforms within the axial channel of Monterey Canyon, offshore California. Geosphere 6, 755–774. https://doi.org/10.1130/GES00527.1.

Paull, C.K., Caress, D.W., Ussler III, W., Lundsten, E., Meiner-Johnson, M., 2011. High-resolution bathymetry of the axial channels within Monterey and Soquel submarine canyons, offshore Central California. Geosphere 7, 1077–1101. https://doi.org/10.1130/GES00636.1.

Paull, C.K., Caress, D.W., Lundsten, E., Gwiazda, R., Anderson, K., McGann, M., Conrad, J., Edwards, B., Sumner, E.J., 2013. Anatomy of the La Jolla Submarine Canyon system; offshore southern California. Mar. Geol. 335, 16–34. https://doi.org/10.1016/j.margeo.2012.10.003.

Paull, C.K., McGann, M., Sumner, E.J., Barnes, P.M., Lundsten, E.M., Anderson, K., Gwiazda, R., Edwards, B., Caress, D.W., 2014. Sub-decadal turbidite frequency during the early Holocene: Eel Fan, offshore northern California. Geology 42, 855–858. https://doi.org/10.1130/G35768.1.

Peakall, J., McCaffrey, B., Kneller, B., 2000. A process model for the evolution, morphology, and architecture of sinuous submarine channels. J. Sediment. Res. 70, 434–448. https://doi.org/10.1306/2DC4091C-0E47-11D7-8643000102C1865D.

Pérez-Belzuz, F., Alonso, B., 2000. Evolución sedimentaria reciente de dos sistemas turbidíticos del área de Motril (NE Alborán). Parte II: sistema turbidítico de Sacratif. Geotemas 1, 207–211.

Pérez-Belzuz, F., Alonso, B., Ercilla, G., 2000. Modelos de sistemas turbidíticos en el Área de Motril (NE Alborán). Geotemas 1, 213–216.

Piper, D.J.W., Normark, W.R., 1983. Turbidite depositional patterns and flow characteristics, Navy depositional lobe, California Borderland. Sedimentology 30, 681–694. https://doi.org/10.1111/j.1365-3091.1983.tb00702.x.

Piper, D.J.W., Savoye, B., 1993. Processes of late quaternary turbidity current flow and deposition on the Var deep-sea fan, north-West Mediterranean Sea. Sedimentology 40, 557–582. https://doi.org/10.1111/j.1365-3091.1993.tb01350.x.

Platt, J.P., Vissers, R.L.M., 1986. Extensional collapse of thickened continental lithosphere: a working hypothesis for the Alboran Sea and Gibraltar Arc. Geology 17, 540–543. https://doi.org/10.1130/0091-7613(1989)017%3C0540:ECOTCL%3E2.3.CO;2.

Pohl, F., Eggenhuisen, J.T., Cartigny, M., Tilston, M.C., 2022. Initiation of deposition in supercritical turbidity currents downstream of a slope break. Sedimentology 1–55. https://doi.org/10.31223/X5M35X.

Posamentier, H., Walker, R., 2006. Deep-water turbidites and submarine fans. In: Walker, R.G. (Ed.), Posamentier, H. SEPM Special Publication, Facies Models Revisited, pp. 397–520. https://doi.org/10.2110/pec.06.84.0399.

Pratson, L.F., Ryan, W.B.F., Mountain, G.S., Twichell, D.C., 1994. Submarine canyon initiation by downslope-eroding sediment flows: evidence in late Cenozoic strata on the New Jersey continental slope. Geol. Soc. Am. Bull. 106, 395–412. https://doi.org/10.1130/0016-7606(1994)106%3C0395:SCIBDE%3E2.3.CO;2.

Puig, P., Greenan, B.J.W., Li, M.Z., Prescott, R.H., Piper, D.J.W., 2013. Sediment transport processes at the head of Halibut Canyon, eastern Canada margin: an interplay between internal tides and dense shelf-water cascading. Mar. Geol. 341, 14–28. https://doi.org/10.1016/j.margeo.2013.05.004.

Puig, P., Palanques, A., Martín, J., 2014. Contemporary sediment-transport processes in submarine canyons. Annu. Rev. Mar. Sci. 6, 53–77. https://doi.org/10.1146/annurev-marine-010213-135037.

Rogers, K.G., Goodbred, S.L., Khan, S.R., 2015. Shelf-to-canyon connections: transportrelated morphology and mass balance at the shallow-headed, rapidly aggrading Swatch of no Ground (Bay of Bengal). Mar. Geol. 369, 288–299. https://doi.org/10.1016/j.margeo.2015.09.011.

Saldías, G.S., Allen, S.E., 2020. The influence of a submarine canyon on the circulation and cross-shore exchanges around an upwelling front. J. Phys. Oceanogr. 50, 1677–1698. https://doi.org/10.1175/JPO-D-19-0130.1.

Scacchia, E., Tinterri, R., Gamberi, F., 2022. The Influence of Channel Planform and Slope Topography on Turbidity Current Overbank Processes: the example of the Acquarone Fan (Southeastern Tyrrhenian Sea). Front. Earth Sci. 9, 1–22. https://doi.org/10.3389/feart.2021.785164.

Schattner, U., Lazar, M., 2016. Hierarchy of source-to-sink systems — example from the Nile distribution across the eastern Mediterranean. Sediment. Geol. 343, 119–131. https://doi.org/10.1016/j.sedgeo.2016.08.006.

Serrano, M.A., Díez-Minguito, M., Valle-Levinson, A., Ortega-Sanchez, M., 2020. Circulation in a short, Microtidal Submarine Canyon in the Alborán Sea. J. Coast. Res. 95, 1531–1535. https://doi.org/10.2112/SI95-295.1.

Shepard, F.P., 1981. Submarine canyons; multiple causes and long-time persistence. Am. Assoc. Pet. Geol. Bull. 65, 1062–1077. https://doi.org/10.1130/0016-7606(1994)106%3C0395:SCIBDE%3E2.3.CO;2.

Slootman, A., Cartigny, M.J.B., 2020. Cyclic steps: Review and aggradation-based classification. Earth Sci. Rev. 201, 102949. https://doi.org/10.1016/j.earscirev.2019.102949.

Smith, D.P., Ruiz, G., Kvitek, R., Iampietro, P.J., 2005. Semi-annual patterns of erosion and deposition in upper Monterey Canyon from serial multibeam bathymetry. Geol. Soc. Am. Bull. 117, 1123–1133. https://doi.org/10.1130/B25510.1.

Smith, D.P., Kvitek, R., Iampietro, P.J., Wong, K., 2007. Twenty-nine months of geomorphic change in upper Monterey Canyon (2002–2005). Mar. Geol. 236, 79–94. https://doi.org/10.1016/j.margeo.2006.09.024.

Smith, M.E., Werner, S.H., Buscombe, D., Finnegan, N.J., Sumner, E.J., Mueller, E.R., 2018. Seeking the shore: evidence for active submarine canyon head incision due to coarse sediment supply and focusing of wave energy. Geophys. Res. Lett. 45, 12,403–12,413. https://doi.org/10.1029/2018GL080396.

Sømme, T.O., Helland-Hansen, W., Martinsen, O.J., Thurmond, J.B., 2009. Relationships between morphological and sedimentological parameters in source-to-sink systems: a basis for predicting semi-quantitative characteristics in subsurface systems. Basin Res. 21, 361–387. https://doi.org/10.1111/j.1365-2117.2009.00397.x.

Spinewine, B., Sequeiros, O.E., Garcia, M.H., Beaubouef, R.T., Sun, T., Savoye, B., Parker, G., 2009. Experiments on wedge-shaped deep sea sedimentary deposits in minibasins and/or on channel levees emplaced by turbidty currents. Part II. J. Sed. Res. 79, 608–628. https://doi.org/10.2110/jsr.2009.064.

Stacey, C.D., Hill, P.R., Talling, P.J., Enkin, R.J., Hughes Clarke, J., Lintern, D.G., 2019. How turbidity current frequency and character varies down a fjord-delta system: Combining direct monitoring, deposits and seismic data. Sedimentology 66, 1–31. https://doi.org/10.1111/sed.12488.

Stanley, D.J., Kelling, G., Vera, J.A., Sheng, H., 1975. Sands in the Alboran Sea: a Model of Input in a Deep Marine Basin. Sm. C. Earth Sc. 15, 1–51. https://doi.org/10.5479/si.00810274.15.1.

Sumner, E.J., Peakall, J., Parsons, D.R., Wynn, R.B., Darby, S.E., Dorrell, R.M., McPhail, S.D., Perrett, J., Webb, A., White, D., 2013. First direct measurements of hydraulic jumps in an active submarine density current. Geophys. Res. Lett. 40, 5904–5908. https://doi.org/10.1002/2013GL057862.

Sun, T., Parker, G., 2005. Transportational cyclic steps created by flow over an erodible bed. Part 2. Theory and numerical simulation. J. Hydraul. Res. 43, 502–514. https://doi.org/10.1080/00221680509500148.

Sun, Y., Wang, D., Canals, M., Alves, T.M., Wang, W., Zhu, Y., Qin, Y., Zeng, F., Zheng, Y., 2023. Bedform evolution along a submarine canyon in the South China Sea: New insights from an autonomous underwater vehicle survey. Sedimentology 13152. https://doi.org/10.1111/sed.13152.

Sylvester, Z., Deptuck, M., Prather, B., Pirmez, C., O'Byrne, C., Mohrig, D., Van Hoorn, B., Wynn, R., 2012. Seismic stratigraphy of a shelf-edge delta and linked slope channels in the northeastern Gulf of Mexico. In: Application of the Principles of Seismic Geomorphology to Continental-Slope and Base-of-Slope Systems: Case Studies from Seafloor and Near-Seafloor Analogues. SEPM, Special Publication, pp. 31–59. https://doi.org/10.2110/pec.12.99.0031.

Symons, W.O., Sumner, E.J., Talling, P.J., Cartigny, M.J., Clare, M.A., 2016. Large-scale sediment waves and scours on the modern seafloor and their implications for the prevalence of supercritical flows. Mar. Geol. 371, 130–148. https://doi.org/10.1016/j.margeo.2015.11.009.

Taki, K., Parker, G., 2005. Transportational cyclic steps created by flow over an erodible bed. Part 1. Experiments. J. Hydraul. Res. 43, 488–501. https://doi.org/10.1080/00221680509500147.

Talling, P.J., Masson, D.G., Sumner, E.J., Malgesini, G., 2012. Subaqueous sediment density flows: depositional processes and deposit types. Sedimentology 59, 1937–2003. https://doi.org/10.1111/j.1365-3091.2012.01353.x.

Talling, P.J., Baker, M.L., Pope, E.L., Ruffell, S.C., Jacinto, R.S., Heijnen, M.S., Hage, S., Simmons, S.M., Hasenhündl, M., Heerema, C.J., McGhee, C., Apprioual, R., Ferrant, A., Cartigny, M.J.B., Parsons, D.R., Clare, M.A., Tshimanga, R.M., Trigg, M. A., Cula, C.A., Faria, R., Gaillot, A., Bola, G., Wallance, D., Griffiths, A., Nunny, R., Urlaub, M., Peirce, C., Burnett, R., Neasham, J., Hilton, R.J., 2022. Longest sediment flows yet measured show how major rivers connect efficiently to deep sea. Nat. Commun. 13, 1–15. https://doi.org/10.1038/s41467-022-31689-3.

Tek, D.E., McArthur, A.D., Poyatos-Moré, M., Colombera, L., Allen, C., Patacci, M., McCaffrey, W.D., 2022. Controls on the architectural evolution of deep-water channel overbank sediment wave fields: insights from the Hikurangi Channel, offshore New Zealand. New Zeal. J. Geol. Geophys. 65, 141–178. https://doi.org/10.1080/00288306.2021.1978509.

Tubau, X., Lastras, G., Canals, M., Micallef, A., Amblas, D., 2013. Significance of the fine drainage pattern for submarine canyon evolution: the Foix Canyon System, Northwestern Mediterranean Sea. Geomorphology 184, 20–37. https://doi.org/10.1016/j.geomorph.2012.11.007.

Tubau, X., Paull, C.K., Lastras, G., Caress, D.W., Canals, M., Lundsten, E., Anderson, K., Gwiazda, R., Amblas, D., 2015. Submarine canyon of Santa Monica Bay, Southern California: Variability in morphology and sedimentary processes. Mar. Geol. 365, 61–79. https://doi.org/10.1016/j.margeo.2015.04.004.

Vangriesheim, A., Khripounoff, A., Crassous, P., 2009. Turbidity events observed in situ along the Congo submarine channel. Deep. Res. Part II Top. Stud. Oceanogr. 56, 2208–2222. https://doi.org/10.1016/j.dsr2.2009.04.004.

Vázquez, J.T., 2001. Estructura del margen continental del Mar de Alborán. PhD Thesis.. Universidad Complutense de Madrid.

Vellinga, A.J., 2019. Froude Supercritical Geophysical Flows: Their Related Bedforms and Frontal Structure. PhD Thesis.. University of Southampton.

Vellinga, A.J., Cartigny, M.J.B., Hansen, E.W.M., Talling, P.J., Clare, M.A., Sumner, E.J., Eggenhuisen, J.T., 2016. Process-based Modelling of Turbidity Currents – from Computational Fluid-dynamics to Depositional Signature. In: Second Conference on Forward Modelling of Sedimentary Systems, Trondheim, 483-00020. https://doi.org/10.3997/2214-4609.201600374.

Vellinga, A.J., Cartigny, M.J.B., Eggenhuisen, J.T., Hansen, E.W.M., 2018. Morphodynamics and depositional signature of low-aggradation cyclic steps: New

insights from a depth-resolved numerical model. Sedimentology 65, 540–560. https://doi.org/10.1111/sed.12391.

von Lom-Keil, H., Spieβ, V., Hopfauf, V., 2002. Fine-grained sediment waves on the western flank of the Zapiola Drift, argentine Basin: evidence for variations in late Quaternary bottom flow activity. Mar. Geol. 192, 239–258. https://doi.org/10.1016/S0025-3227%2802%2900557-1.

Wan, L., Hurter, S., Bianchi, V., Li, P., Wang, J., Salles, T., 2022. The roles and seismic expressions of turbidites and mass transport deposits using stratigraphic forward modeling and seismic forward modeling. J. Asian Earth Sci. 232, 105110. https://doi.org/10.1016/j.jseaes.2022.105110.

Wang, X., Wang, Y., He, M., Chen, W., Zhuo, H., Gao, S., Wang, M., Zhou, J., 2017. Genesis and evolution of the mass transport deposits in the middle segment of the Pearl River canyon, South China Sea: Insights from 3D seismic data. Mar. Petrol. Geol. 88, 555–574. https://doi.org/10.1016/j.marpetgeo.2017.08.036.

Wilkin, J., Cuthbertson, A., Dawson, S., Stow, D., Stephen, K., Nicholson, U., Penna, N., 2023. The response of high density turbidity currents and their deposits to an abrupt channel termination at a slope break: Implications for channel–lobe transition zones. Sedimentology 70, 1164–1194. https://doi.org/10.1111/sed.13073.

Wunsch, M., Betzler, C., Lindhorst, S., Lüudmann, T., Eberli, G.P., 2017. Sedimentary dynamics along carbonate slopes (Bahamas archipelago). Sedimentology 64, 631–657. https://doi.org/10.1111/sed.12317.

Wynn, R.B., Stow, D.A.V., 2002. Classification and characterisation of deep-water sediment waves. Mar. Geol. 192, 7–22. https://doi.org/10.1016/S0025-3227(02)00547-9.

Wynn, R.B., Weaver, P.P., Ercilla, G., Stow, D.A., Masson, D.G., 2000. Sedimentary processes in the selvage sediment-wave field, NE Atlantic: new insights into the formation of sediment waves by turbidity currents. Sedimentology 47, 1181–1197.

Wynn, R.B., Kenyon, N.H., Masson, D.G., Stow, D.A.V., Weaver, P.P.E., 2002. Characterization and recognition of deep-water channel-lobe transition zones. AAPG Bull. 86, 1441–1462. https://doi.org/10.1306/61eedcc4-173e-11d7-8645000102c1865d.

Xu, J.P., Wong, F.L., Kvitek, R., Smith, D.P., Paull, C.K., 2008. Sandwave migration in Monterey Submarine Canyon, Central California. Mar. Geol. 248, 193–212. https://doi.org/10.1016/j.margeo.2007.11.005.

Xu, J.P., Swarzenski, P.W., Noble, M., Li, A.C., 2010. Event-driven sediment flux in Hueneme and Mugu submarine canyons, southern California. Mar. Geol. 269, 74–88. https://doi.org/10.1016/j.margeo.2009.12.007.

Xu, J.P., Barry, J.P., Paull, C.K., 2013. Small-scale turbidity currents in a big submarine canyon. Geology 41, 143–146. https://doi.org/10.1130/G33727.1.

Zhong, G., Cartigny, M.J., Kuang, Z., Wang, L., 2015. Cyclic steps along the South Taiwan Shoal and West Penghu submarine canyons on the northeastern continental slope of the South China Sea. Geol. Soc. Am. Bull. 127, 804–824. https://doi.org/10.1130/B31003.1.

Zhou, W., Chiarella, D., Zhuo, H., Wang, Y., Tang, W., Zou, M., Xu, Q., 2021. Genesis and evolution of large-scale sediment waves in submarine canyons since the Penultimate Glacial Maximum (ca. 140 ka), northern South China Sea margin. Mar. Petrol. Geol. 134, 105381. https://doi.org/10.1016/j.marpetgeo.2021.105381.

Zhu, M., Graham, S., Pang, X., McHargue, T., 2010. Characteristics of migrating submarine canyons from the middle Miocene to present: Implications for paleoceanographic circulation, northern South China Sea. Mar. Petrol. Geol. 27, 307–319. https://doi.org/10.1016/j.marpetgeo.2009.05.005.